Spaceplates: The Final Frontier in Compressing Optical Systems

Michael DelMastro

Thesis submitted to the University of Ottawa
in partial fulfilment of the requirements for the
MSc degree in Physics

Under the supervision of
Jeff S. Lundeen

Department of Physics
Faculty of Science
University of Ottawa

Abstract

In the last decade, metalenses have become an increasingly popular topic of research, partly due to their ability to reduce the physical space that would otherwise by occupied by traditional lenses, thereby reducing the length of the optical system. However, metalenses do not reduce the largest contributor to optical system length: the propagation of the light between optical elements. We present a novel optic, which we call a "spaceplate," that can replicate propagation distance of light greater than its thickness, without changing the magnification. We demonstrate the capabilities of spaceplates via proof of concept experiments that use two distinct types of spaceplate; the "low-index" spaceplate is based on Snell's Law, while the "uniaxial" spaceplate utilizes the anisotropy of birefringent crystals. The 11 mm thick low-index spaceplate reduced light propagation by (4.7 ± 0.2) mm and the 15 mm thick uniaxial spaceplate reduced light propagation by (1.2 ± 0.2) mm. Future spaceplates, especially in conjunction with metalenses, could vastly decrease the length of optical systems, including imaging systems like cameras, and has the potential to make such systems monolithic.

Acknowledgements

First, I would like to thank my supervisor, Jeff Lundeen, who has instilled in me a deep appreciation and understanding of the scientific method. His support was invaluable for me to succeed in this research and in my education. The experience I have gained in his group has been indispensable.

I also want to thank all of the current and former members of the Lundeen Lab team for their help and companionship in the lab. It has been a humbling experience working with such an intelligent group of people. In particular, I'd like to thank Lambert Giner for his crucial technical support. Thanks to Kat Bearne for introducing me to the lab way back in 2018.

Thank you to the CERC group for giving me a venue to develop my skills. Thanks to my officemates, Sisira, Tuhin, and Kaustubh. Special thanks to Orad Reshef, who taught me the essential skills that I needed to complete this degree. His expertise was indispensable for this research. Our many great conversations about physics and politics were always enlightening.

Thanks to my friends, Stephen, Emily, and Codey, for many fun video game sessions. Thank you to my friend Stephanie, who I can talk to about anything and everything. I want to thank my boyfriend, Ryan, and our feline son, Clarence. Ryan's constant love and support has been vital to me, especially during this pandemic. His unwavering encouragement doubtlessly helped me achieve my goals. Clarence's companionship was much appreciated and he is a very good cat.

Most importantly, I want to thank my parents, June and Patrick, who consistently encouraged and enabled me to get an education. I cannot thank them enough for their unconditional love and support. Without them, this thesis would not have been possible.

Contents

Author Contributions

This thesis presents the work of several individuals. The original concept of the spaceplate was developed by Jeff Lundeen and Orad Reshef. The majority of the derivations were done by Jeff Lundeen. Robert Boyd suggested the concept of using ENZ materials as a spaceplate, which inspired the broader concept of low-index spaceplates, and Orad Reshef proved that ENZ spaceplates work in theory. Katherine Bearne assembled the initial setup and performed early measurements. Lambert Giner developed the code used to take measurements (LabView) and process data (MATLAB). Orad Reshef developed additional MATLAB programs and made edits to Lambert's code. Orad also assisted me in the lab on numerous occasions. I took all of the measurements presented in this thesis. All of the figures were made by me, unless otherwise cited. I also assembled and aligned much of the setup used in these experiments. Lastly, I made some minor contributions to a few derivations and to some of the MATLAB code.

Chapter 1

Reducing the Length of Optical Systems

Since the invention of optical systems, there have been numerous attempts at reducing their length. An optical system is a series of optical components (lenses, mirrors, polarizers, etc.) through which light propagates to achieve a certain goal, such as imaging. Reducing the length of such systems is important because it reduces manufacturing costs and makes them more practical to transport and operate.

In this thesis, I will introduce a novel optic that is capable of reducing the amount of physical space required for light to propagate. We call this optic a "spaceplate" and it will be introduced in earnest at the end of this chapter. But first, to better understand the concept of a spaceplate, it is useful know what it is not. We will explore other methods of reducing optical system length, their advantages and disadvantages, and how a spaceplate accomplishes this differently.

1.1 Multi-optic Systems

Currently, one of the most common methods of decreasing the length of an optical system is by using a multi-optic system. A simple example of this is a telephoto lens system. This traditionally consists of a convex lens followed by a concave lens, separated by a certain distance. As an aside, the spherical aberration created by the convex lens is largely corrected by the concave lens. In practice, the length of a telephoto lens system can only be reduced to about 80% of its effective focal length [1], however this may not be a fundamental limitation. The total system length that

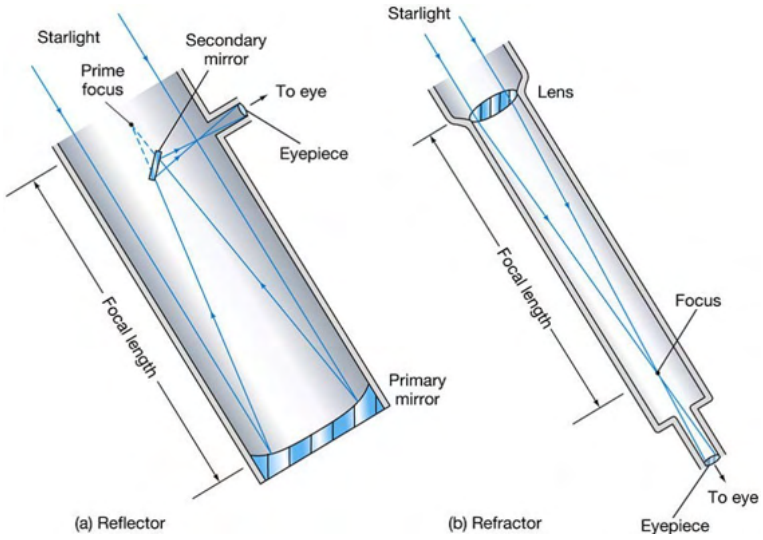

Figure 1.1: **(a)** A reflecting telescope compared to **(b)** a refracting telescope. Note that the refracting telescope is longer than the reflecting telescope in relation to the focal length [2].

can be reduced via telephoto lenses is limited by minimum focal lengths, aberrations, and lens alignment. Importantly, there is a minimum separation between the lenses that is dependent on their focal lengths, which is the main limitation on how much the length of the system can be reduced.

Using a mirror system instead of a lens system has been effective at reducing the length of optical devices such as telescopes. A refracting telescope consists of at least two lenses, which have a net magnification M greater than unity. By replacing these lenses with curved mirrors, we get a reflecting telescope which takes up less space along the direction of the incoming light (Fig. 1.1). One way to think about reflecting telescopes is that you are taking the light propagation from a traditional refracting telescope and folding it in space.

Reflecting telescopes have the added benefit of avoiding chromatic aberrations. Also, they can have larger apertures, since mirrors can be more easily fabricated with large diameters compared to lenses. However, there are several disadvantages which need to be taken into account. Firstly, most reflective telescopes have a secondary mirror which must be mounted along the central axis, meaning that it blocks some of the incoming light. In particular, it usually is held by one or more support vanes, which result in diffraction spikes in the image. Additionally, it is preferable to use parabolic mirrors instead of spherical mirrors to avoid spherical aberrations. Since parabolic

mirrors are much more difficult to manufacture, that makes reflective telescopes generally more expensive than refractive telescopes. Furthermore, parabolic mirrors can still introduce other aberrations such as coma and astigmatism [3].

Unfortunately, all lenses and curved mirrors have a common problem when it comes to reducing the length of optical systems. They all affect the magnification of the image. While there are optical systems whose total magnification M is equal to unity, systems like this are relatively long due to the necessary propagation distance between the lenses, as mentioned with the telephoto lens system. More complicated optical systems, which are required in high-precision instruments, take up even more space and can be exceptionally heavy.

1.2 Reducing Focal Length

A simpler method of reducing the length of optical systems is to use lenses of a short focal length. If your lens has a focal length f smaller than the distance between the lens and the object p, then as you decrease focal length, the distance between the lens and the image q will also decrease, thus reducing the overall length of the system. This simple relationship can be found by rearranging the thin lens equation,

$$\frac{1}{f} = \frac{1}{p} + \frac{1}{q}\,. \tag{1.1}$$

But how do we achieve lower focal lengths? The focal length of a lens is dependent on its index of refraction n, the thickness of the lens d, and the curvature of the lens. For spherical lenses, this relationship is described by the lensmaker's equation,

$$\frac{1}{f} = (n-1)\left[\frac{1}{R_1} - \frac{1}{R_2} + \frac{(n-1)d}{nR_1R_2}\right], \tag{1.2}$$

where R_1 and R_2 are the radii of curvature for the front and back surface of the lens, respectively [3]. These equations assume that the background medium is air or vacuum (free space).

The most common way to reduce the focal length is to reduce the radius of curvature. As a result, it is often necessary to increase the central thickness of convex lenses in order to achieve a lens with a sufficiently large diameter. Conversely, for concave lenses, it's necessary to increase

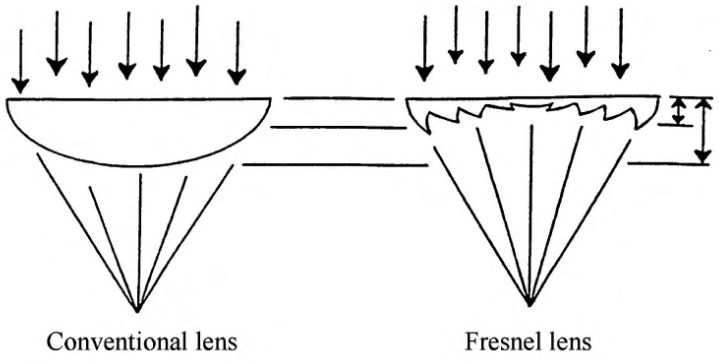

Figure 1.2: A traditional lens compared to Fresnel lens. The thickness of the Fresnel lens is less than that of the traditional lens [5].

the edge thickness to account for the smaller magnitude of the radius of curvature. The increase in lens material that the light must propagate through intensifies the severity of chromatic aberrations.

1.3 Fresnel Lenses

Increasing the thickness of a lens also increases its absorption, weight, and cost. This led to the development of the Fresnel lens, which cuts out unnecessary lens material while retaining the same surface curvature and, therefore, the same focal length. Fresnel lenses consist of concentric sections which have the same surface curvature a traditional lens, which results in sudden changes in thickness at certain radii (Fig. 1.2). The reduction in the thickness of the lens results in a slight reduction in the overall length of the optical system. These types of lenses are famously used in lighthouses, but have also found use in overhead projectors, viewfinders, solar concentrators [4,5], and VR headsets [6].

However, there are some issues with Fresnel lenses which make them unsuitable for certain applications. Scattering occurs at the edges of each section, which can create artifacts in the image. These edges make them more difficult and expensive to manufacture, compared to a simple spherical lens. Furthermore, the edges can collect dust and other particulate matter more than a typical lens. This results in additional scattering and makes Fresnel lenses difficult to clean. Lastly, they cannot achieve high-resolution imaging without post-processing [7].

1.4 Metalenses

We can remedy some of these issues by taking the concept of a Fresnel lens to its logical extreme. Namely, how thin can we make a Fresnel lens? The advent of metasurfaces has answered that question with metalenses, which are microscale to nanoscale thick lenses (Fig. 1.3). A metasurface is a thin film with sub-wavelength scale periodic structures which are capable of altering the amplitude and phase of light in otherwise impossible ways [8]. A metalens is a type of metasurface which applies a position-dependent phase shift, as a typical lens does. Generally, a lens will impart onto the incoming light a phase shift of

$$\phi(r) = \frac{2\pi}{\lambda} d(r)\,, \tag{1.3}$$

where r is the radial position, λ is the wavelength of the incoming light, and $d(r)$ is the thickness of the lens as a function of radius. This function is different for every type of lens. More specifically, a perfect lens will impart a phase of

$$\phi(r) = \frac{2\pi}{\lambda} \left(\sqrt{r^2 + f^2} - f \right) . \tag{1.4}$$

Indeed metalenses can impart this same phase shift within a much smaller thickness than a traditional glass lens [9].

This is achieved via nanostructures, each of which acts as a point source when light is incident on the metalens. These nanostructures are typically made of high refractive index ($n > 2$) dielectric materials, such as Si [10], GaN [11], and TiO_2 [12, 13]. This is advantageous since they result in very low absorption losses. The nanostructures can be made into various shapes including cylinders [10], V-shapes [14], rectangular prisms [12], etc. These structures are separated by distances smaller than the wavelength of light. Metalens designs are often tested in FDTD (finite-difference time-domain) simulations, which accurately predict a metalens's performance in reality. Impressively, metalenses have demonstrated imaging numerous times, including at visible wavelengths [12, 15–17]. This makes it possible for such lenses to be used in cameras and many other imaging systems.

The way in which metalenses are fabricated presents an opportunity for mass production,

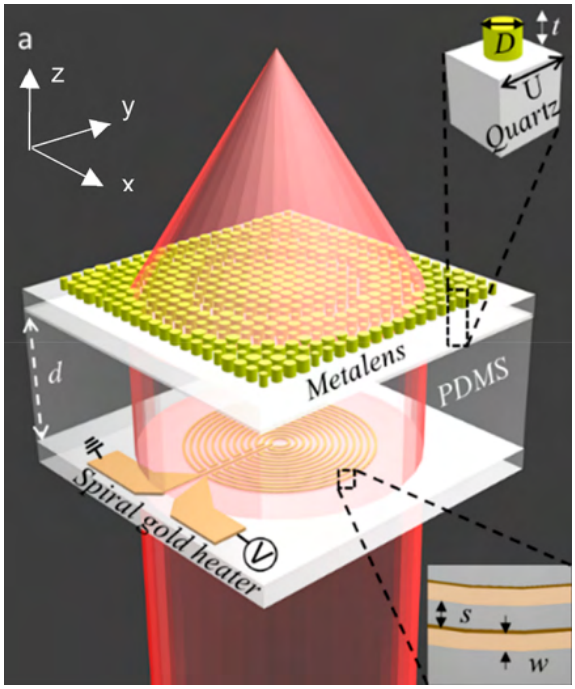

Figure 1.3: An example of a metalens which uses silicon cylindrical nanostructures on a quartz substrate. Figure adapted from Ref. [10].

similar to the method of manufacturing computer chips. The base is a substrate upon which the nanostructures are built. The substrate can be made of glass, calcite, fused silica, or any other solid, stable material which is transparent to the wavelength(s) of light for which the metalens is designed. Then, the material that comprises the nanostructures is deposited onto the substrate. Various lithographic techniques are used to etch the nanostructures into this material and remove the excess. Finally, these metalenses are tested experimentally, usually resulting in strong agreement with simulations. Current fabrication techniques are simple in concept, but can be costly. Recently, low-cost methods have been developed which can bring about commercial metalenses [13].

1.5 Glass Plates

There is an optic which can replicate large amounts of free space propagation, but only in the context of collimated light, meaning that the light is neither converging nor diverging. That

optic is a simple glass plate (or any slab of a transparent medium with an index of refraction greater than that of air). In an interferometer with arms of equal length, light will accumulate more phase in one of the arms by inserting a glass plate into the path of the beam [18]. This is related to the concept of optical path length, OPL $= ns$, where s is the length of the path the light ray takes [3]. From this, we know that light propagation in a high-index medium is equal to a longer propagation in free space.

When attempting to apply this principle to non-collimated light, it has the opposite effect of taking up more space along the direction of propagation than it otherwise would without the glass plate. Let's take the marginal ray of a beam of light focusing at an angle θ_1 with respect to the normal of the glass plate as it travels through free space. When the ray transmits through the plate, which has a higher refractive index than the surrounding medium, it bends towards the normal, propagating at a smaller angle θ_2. This is easily determined from Snell's Law [3],

$$n_1 \sin\theta_1 = n_2 \sin\theta_2 \,. \tag{1.5}$$

However, this results in the beam focussing farther away than it would if the glass plate were not present (Fig. 1.4). In effect, this has added additional propagation distance. Therefore, if a beam is not collimated, a glass plate will not reduce the length of the system and, in fact, adds additional length.

1.6 Spaceplates

The main aspect of optical systems which has not been reduced in length is the propagation distance between each optic. This is often the principal limiting factor when it comes to compressing these kinds of systems. In nearly any optical system, from cell phone cameras to massive telescopes, there is a great deal of empty space through which the light must propagate in order for the optical system to function. These propagation distances make optical devices unnecessarily large. I will present a novel optic which can be inserted into an optical system in order to reduce the required propagation distance of the light. In later chapters, I will present experimental data which verifies the effects of this optic.

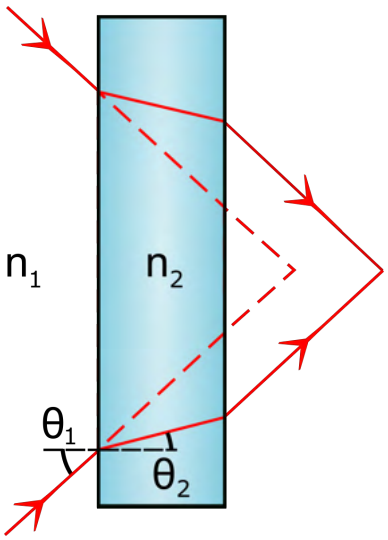

Figure 1.4: The marginal rays (red solid lines) of a converging beam of light passing through a plate of index $n_2 > n_1$, such as a glass plate in air. Note that the light comes to a focus at a distance further away than it would without the plate (red dashed lines).

This optic, which we call a "spaceplate," replicates a certain propagation distance d_{eff} for light within its thickness $d < d_{\text{eff}}$. Figure 1.5 depicts a light ray approaching the spaceplate at an angle θ with respect to the normal of the plate. In the spaceplate, it travels at a larger angle θ_{SP}. This results in a transverse displacement w of the light. Importantly, the ray would have travelled a transverse distance w if it had propagated a longitudinal distance d_{eff} without the spaceplate. Finally, once it exits the spaceplate, the light once again travels at the original angle of θ. Since the entrance and exit faces are parallel, this means that the exiting light ray propagates in its original direction and, therefore, magnification is not affected. The ray has been laterally displaced from its original trajectory by Δx, which is closely related to w. This relationship will be explored in the next chapter.

The combination of the above properties means that the spaceplate has effectively compressed the propagation of a longer distance d_{eff} into a smaller distance d. From this, we can quantify the effectiveness of a given spaceplate. We define a compression factor, $\mathcal{R} \equiv d_{\text{eff}}/d$. But since we do not know how much space a given spaceplate will replicate, how do we calculate this compression factor? There will be other equations for $\mathcal{R}$ which will be derived in the following chapter.

When we apply this effect to a focusing beam of light, it becomes clearer how spaceplates

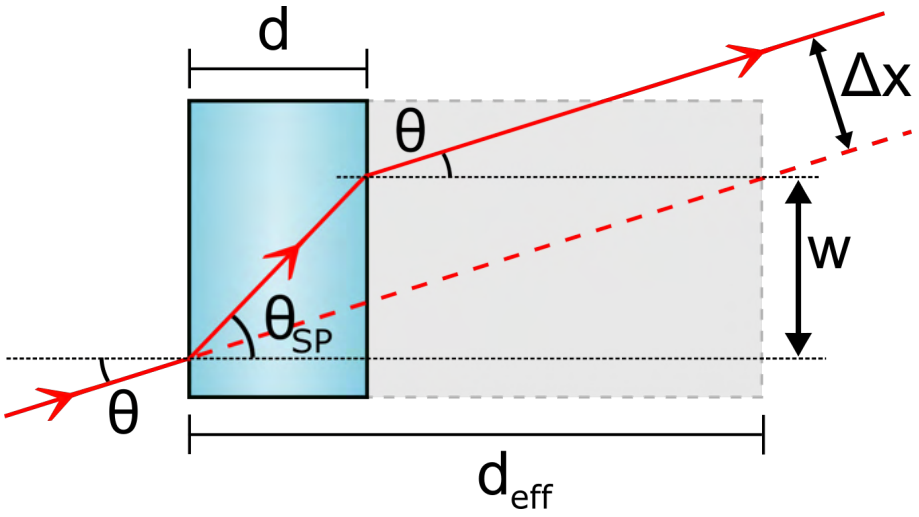

Figure 1.5: The basic functionality of a spaceplate. The blue rectangle is the side view of a spaceplate. The grey rectangle shows the amount of space being replaced by the spaceplate.

can reduce the space required in an optical system. Figure 1.6.a depicts a collimated beam of light incident on a convex lens, which then forms the beam waist at the focal point. The beam waist is the position at which the beam has its smallest diameter. When a spaceplate is inserted into the path of the focusing light (Fig. 1.6.b), the beam waist gets shifted by a distance Δ. We define this shift to be negative, since the light is propagating along the positive direction of the z axis. Any optics later in the system simply need to be translated along z by a distance Δ, which reduces the overall length of the system.

The spaceplate concept can be applied to nearly any optical system. Potential applications include cameras, telescopes, VR headsets, spectrometers, and solar concentrators. A major advantage of the spaceplate is that it can be introduced into an optical system and nothing about the system has to be changed except the spacing of the optics immediately before and after the spaceplate. In other words, we do not require prior knowledge of the system to account for the addition of a spaceplate, unlike with the other methods of reducing optical system length.

The real potential of spaceplates can be optimized if they are used in series with metalenses. Both optics could be combined into a single monolithic device which would achieve the same effect as traditional lenses and free space propagation. Applied to imaging systems, these optics could enable the creation of ultra-thin cameras [19], as depicted in Fig. 1.7. Future developments

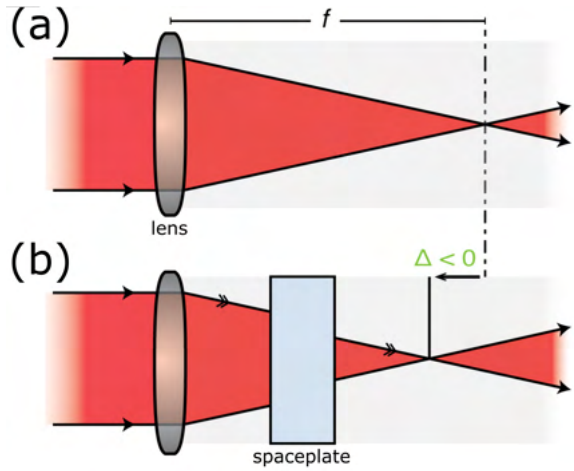

Figure 1.6: **(a)** A light beam being focused through a convex lens in a medium. **(b)** A spaceplate inserted into the path of the focusing beam shifts the beam waist against the direction of propagation by a distance Δ. Figure adapted from Ref. [19].

in spaceplates and metalenses could result in substantial decreases in the length of some optical systems. Systems whose length is on the order of centimetres could be reduced to micrometres.

It is important to consider which properties a spaceplate would need in order to be used in these applications. Firstly, a commercial spaceplate would need to be able to function in free space. Ideally, it would be polarization-independent. For most imaging applications, we would need a decently high numerical aperture, NA$= n \sin\theta$. For context, most cell phone cameras have NA=0.2, while the numerical aperture of professional cameras can vary significantly, usually in the range of 0.02 to 0.36.

In addition, we need to know the wavelengths for which the spaceplate functions. While there are some monochromatic applications, it is preferable for a spaceplate to be broadband. In particular, we would like a spaceplate to be broadband in the visible spectrum, in order for it to be used in most commercial imaging systems. Lastly, we do not want a spaceplate to add any significant aberrations to the system. Our work achieves a few of these properties using two different spaceplate designs, which each have their own advantages and disadvantages.

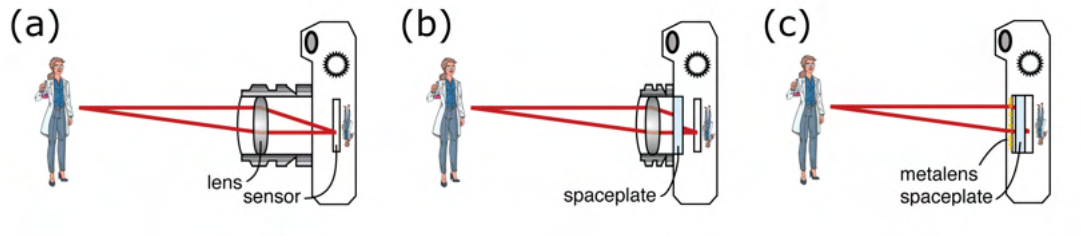

Figure 1.7: A spaceplate's application to cameras. **(a)** A traditional camera. **(b)** A spaceplate inserted into a traditional camera system, thereby reducing the length of the lens barrel. **(c)** A camera where the lens has been replaced with a metalens and a spaceplate has been inserted. Notice that this system is now monolithic. Figure adapted from Ref. [19].

Chapter 2

Theory Describing Homogeneous Spaceplates

There are indeed designs for heterogeneous spaceplates, but those will not be the focus of this thesis. They will be discussed briefly in the Conclusion chapter. Rather, this thesis will describe homogeneous spaceplates. We will find that there are at least two distinct types of homogeneous spaceplate: one that is isotropic and one that is anisotropic. Both will arise as a consequence of the same theory based in Fourier optics.

2.1 Fourier Optics

To understand the mechanism behind the spaceplate effect, we first need to look to Fourier optics, which states that all light waves can be described as the superposition of plane waves. If we take a plane wave travelling in an arbitrary direction $\vec{r}$, we can separate that wave into the product of its three Cartesian components, $E(\vec{r}) = E_x(x)\,E_y(y)\,E_z(z)$, since the components of a plane wave are separable. As such, we can consider each component individually. However, we will need to work in Fourier space, rather than Euclidean space. By taking the Fourier transforms of the fields, we end up with a function dependent on $\vec{k} = (k_x, k_y, k_z)$, which is the wavevector. Its magnitude $k = 2\pi/\lambda$ is known as the angular wavenumber.

The Fourier transfer function $H(\vec{k})$ determines how the transverse spatial distribution of the light field transforms as a function of z, the axis that we define as being normal to the interface of the background medium and the spaceplate. Note that $H(\vec{k})$ is the Fourier transform of the impulse response function $h(\vec{r})$ [20], where the impulse response function is the output of a

system whose input is the Dirac delta function (point source). In the field of optics, the impulse response function is more commonly referred to as the point spread function.

A spaceplate needs to replicate the Fourier transfer function of a slab of free space of thickness d_{eff} within a plate of smaller thickness d. More generally, we can consider light propagating through a background medium whose index of refraction n_{BG} is not necessarily equal to unity. Specifically, we analyze how propagation of light through that medium affects a plane wave with wavevector, $\vec{k}^{\text{BG}} = \vec{k}\, n_{\text{BG}}$.

Considering each component of $\vec{k}^{\text{BG}}$ individually, let's define the transmissive faces of the spaceplate slab to be in the x-y plane. Recall that z is normal to the interface. In general, the phase of a plane wave is $\phi = \vec{k} \cdot \vec{r}$. Thus, the phase of the plane wave at any point along the exit face of the slab is $\phi = k_x^{\text{BG}} x + k_y^{\text{BG}} y + k_z^{\text{BG}} d_{\text{eff}}$, because the spaceplate needs to replicate phase accumulation from $z = 0$ to $z = d_{\text{eff}}$. Since we are only considering spaceplates with flat, smooth, and parallel faces, the spaceplate will conserve the x and y components of the incoming wavevector. It follows that the corresponding phase contributions of the spaceplate in the transverse directions will be identical to those from the propagation in the background medium. As a result, we only need to consider replicating the phase along the z direction.

The corresponding phase accumulation in the background medium is $\phi_{\text{BG}} = k_z^{\text{BG}} d_{\text{eff}}$, where $k_z^{\text{BG}} = k\, n_{\text{BG}} \cos\theta$ and θ is the angle that $\vec{k}$ makes with respect to the z axis. Similarly, propagation inside a homogeneous spaceplate will impart phase $\phi_{\text{SP}} = k_z^{\text{SP}} d$, where $k_z^{\text{SP}} = k\, n_{\text{SP}} \cos\theta_{\text{SP}}$ and θ_{SP} is the angle that $\vec{k}$ makes with respect to the z axis within the spaceplate. The dependence on k_z thereby results in a dependence on θ. We will derive that the homogeneous spaceplate in turn needs to have an angle-dependent index of refraction $n_{\text{SP}}(\theta_{\text{SP}})$.

2.2 Derivation of the Angle-Dependent Refractive Index

Referring back to the Fourier transfer function H, it is known that the transfer function of a slab of free space [20] spanning 0 to z transforms a plane wave as,

$$E(k_x, k_y, z) = H(k_x, k_y, z)\; E(k_x, k_y, 0) = e^{ik_z z} E(k_x, k_y, 0)\,, \tag{2.1}$$

where there is an implicit dependence on the transverse wavevectors in the transfer function via $k_z = \sqrt{k^2 - k_x^2 - k_y^2}$, from the Pythagorean Theorem.

A spaceplate must replicate both the phase from background medium propagation ϕ_{BG} and the angle-independent global offset phase ϕ_{G}. While ϕ_{BG} is the phase accumulated by light propagating through d_{eff} of the background medium, ϕ_{G} is a constant. The majority of optical systems, including imaging systems, are not sensitive to this global offset phase [21] and will therefore grant us a great deal of flexibility in our derivations. The Fourier transfer function of each phase is of the form $e^{i\phi}$. Since Fourier transfer functions are multiplicative,

$$\begin{aligned} e^{i\phi_{\mathrm{SP}}} &= e^{i\phi_{\mathrm{BG}}} e^{i\phi_{\mathrm{G}}} \\ 1 &= e^{i(\phi_{\mathrm{SP}} - \phi_{\mathrm{BG}} - \phi_{\mathrm{G}})} \\ \implies 2\pi m &= \phi_{\mathrm{SP}} - \phi_{\mathrm{BG}} - \phi_{\mathrm{G}} \qquad (2.2) \\ 2\pi m &= k_z^{\mathrm{SP}} d - k_z^{\mathrm{BG}} d_{\mathrm{eff}} - \phi_{\mathrm{G}}, \qquad (2.3) \end{aligned}$$

where m is an integer. This dependency of ϕ_{SP} on an integer allows for a discontinuous function, analogous to a Fresnel lens, except in k-space instead of position space [22,23]. Using the relations $k_z^{\mathrm{SP}} = k^{\mathrm{SP}} \cos\theta_{\mathrm{SP}}$ and $k_z^{\mathrm{BG}}/n_{\mathrm{BG}} = k_z^{\mathrm{SP}}/n_{\mathrm{SP}}(\theta_{\mathrm{SP}})$, we can convert the first term of Eq. (2.3) into

$$k_z^{\mathrm{SP}} d = \tilde{n}(\theta_{\mathrm{SP}}) k^{\mathrm{BG}} d \cos\theta_{\mathrm{SP}}, \qquad (2.4)$$

where $\tilde{n}(\theta_{\mathrm{SP}}) \equiv n_{\mathrm{SP}}(\theta_{\mathrm{SP}})/n_{\mathrm{BG}}$. We can then find how the second term of Eq. (2.3) depends on θ_{SP} by using the conservation of the transverse component of the wavevector,

$$\begin{aligned} k_\perp &\equiv \sqrt{\left(k_x^{\mathrm{BG}}\right)^2 + \left(k_y^{\mathrm{BG}}\right)^2} \\ &= \sqrt{\left(k_x^{\mathrm{SP}}\right)^2 + \left(k_y^{\mathrm{SP}}\right)^2} \\ &= k_{\mathrm{SP}} \sin\theta_{\mathrm{SP}} \\ &= k_{\mathrm{BG}}\, \tilde{n}(\theta_{\mathrm{SP}}) \sin\theta_{\mathrm{SP}}\,, \qquad (2.5) \end{aligned}$$

as well as $k_\perp^2 = (k^{\mathrm{BG}})^2 - (k_z^{\mathrm{BG}})^2$. The second term of Eq. (2.3) can then be expressed as

$$\begin{aligned} k_z^{\mathrm{BG}} d_{\mathrm{eff}} &= d_{\mathrm{eff}} \sqrt{(k^{\mathrm{BG}})^2 - k_\perp^2} \\ &= k^{\mathrm{BG}}\, d_{\mathrm{eff}} \sqrt{1 - \tilde{n}^2(\theta_{\mathrm{SP}}) \sin^2 \theta_{\mathrm{SP}}}\,. \end{aligned} \tag{2.6}$$

Inserting both Eq. (2.4) and Eq. (2.6) into Eq. (2.3) give us the relation

$$2\pi m = \tilde{n}(\theta_{\mathrm{SP}}) k^{\mathrm{BG}} d \cos\theta_{\mathrm{SP}} - k^{\mathrm{BG}}\, d_{\mathrm{eff}} \sqrt{1 - \tilde{n}^2(\theta_{\mathrm{SP}}) \sin^2 \theta_{\mathrm{SP}}} - \phi_{\mathrm{G}}. \tag{2.7}$$

We can use the formula $k^{\mathrm{BG}} = 2\pi n_{\mathrm{BG}}/\lambda$, where λ is the vacuum wavelength, and rearrange Eq. (2.7) to define a new parameter,

$$C \equiv \left(m + \frac{\phi_{\mathrm{G}}}{2\pi}\right) \frac{\lambda}{n_{\mathrm{BG}} d} = \tilde{n}(\theta_{\mathrm{SP}}) \cos\theta_{\mathrm{SP}} - \mathcal{R} \sqrt{1 - \tilde{n}^2(\theta_{\mathrm{SP}}) \sin^2 \theta_{\mathrm{SP}}}\,. \tag{2.8}$$

Recall that $\mathcal{R} \equiv d_{\mathrm{eff}}/d$. To get a better grasp of what C represents physically, we can use Eq. (2.2) to express it as

$$C = \frac{2\pi m + \phi_{\mathrm{G}}}{k^{\mathrm{BG}} d} = \frac{\phi_{\mathrm{SP}} - \phi_{\mathrm{BG}}(z = d_{\mathrm{eff}})}{\phi_{\mathrm{BG}}(z = d)}, \tag{2.9}$$

which demonstrates that C is simply the ratio of phases. The denominator, $\phi_{\mathrm{BG}}(z = d)$, is the the phase accumulated if the spaceplate were absent, leaving just a region of background medium of thickness d. The numerator is the phase created by the spaceplate, minus the background phase accumulated over d_{eff}. The dependence on ϕ_{G} and m provides significant freedom in choosing values of C and, in turn, potential designs for homogeneous spaceplates.

Solving Eq. (2.9) for $\tilde{n}(\theta_{\mathrm{SP}})$ yields the general solution for the index of refraction of any homogeneous spaceplate,

$$\tilde{n}(\theta_{\mathrm{SP}}) \equiv \frac{n(\theta_{\mathrm{SP}})}{n_{\mathrm{BG}}} = \frac{C \pm \sqrt{C^2 + (\mathcal{R}^2 - C^2)(1 + \mathcal{R}^2 \tan^2 \theta_{\mathrm{SP}})}}{\cos\theta_{\mathrm{SP}} (1 + \mathcal{R}^2 \tan^2 \theta_{\mathrm{SP}})}. \tag{2.10}$$

This presents us with a family of solutions to the above general equation, each of which has a different value for C. Some of them are plotted in Fig. 2.1. Although we only plot the positive

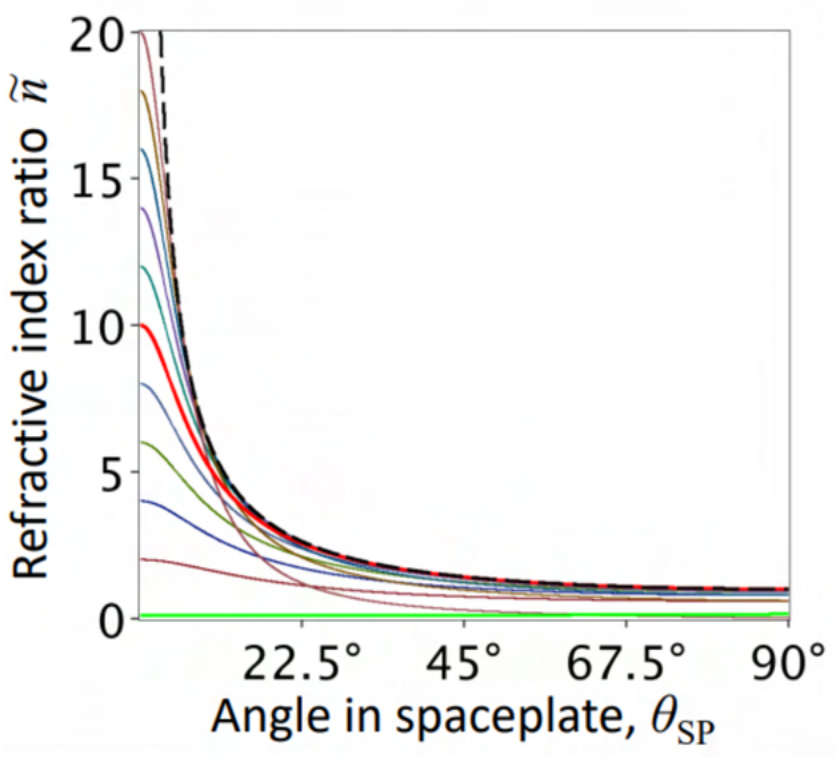

Figure 2.1: Plot of some select solutions to Eq. (2.10) for a compression factor $\mathcal{R} = 10$. Each of these solutions is an even function. The green curve is the low-index solution. The red curve is the uniaxial solution. The black dotted line is the limiting case. Figure adapted from the Supplementary Information of Ref. [19].

solutions here, it is important to note that there exist negative index solutions to this general equation as well. While there are dozens of valid solutions to this equation, we know of only two which can describe a known physical system.

2.2.1 Low-Index Solution

If, in this general solution, we set $C = \mathcal{R}^{-1} - \mathcal{R}$ and take the positive term, we find that it becomes

$$\tilde{n}(\theta_{\mathrm{SP}}) = \frac{\mathcal{R}^{-1} - \mathcal{R} + \sqrt{\mathcal{R}^2 + (2\mathcal{R}^2 - 1)\tan^2\theta_{\mathrm{SP}}}}{\cos\theta_{\mathrm{SP}}\left(1 + \mathcal{R}^2\tan^2\theta_{\mathrm{SP}}\right)}. \tag{2.11}$$

While the index of refraction appears to have a somewhat complicated dependence on θ_{SP}, it is approximately constant. For this reason, it approximates the physical system of a spaceplate with a constant index of refraction. We will derive later that the compression factor for the low-index solution is $\mathcal{R}_{\mathrm{LI}} = n_{\mathrm{BG}}/n_{\mathrm{SP}}$. In order to get a value of $\mathcal{R}_{\mathrm{LI}} > 1$, the spaceplate must have an index of refraction that is lower than that of the background medium (i.e. $n_{\mathrm{SP}} < n_{\mathrm{BG}}$).

However, it is known that for light going from a high-index medium to a low-index medium, there is a critical angle beyond which the light will be entirely reflected (total internal reflection). Applied to a low-index spaceplate, this critical angle is $\theta_{\mathrm{crit}} = \arcsin\left(n_{\mathrm{SP}}/n_{\mathrm{BG}}\right)$. This fundamentally limits the numerical aperture (NA) of any low-index spaceplate. Furthermore, as the angle of the incident light approaches this critical angle, aberrations become more severe. This aspect of low-index spaceplates will be explored in the discussion of beam walk-off Δx.

2.2.2 Uniaxial Solution

Let's instead take Eq. (2.10) and set $C = 0$. Again taking the positive term, we find that this simplifies to

$$\tilde{n}(\theta_{\mathrm{SP}}) = \frac{\mathcal{R}}{\cos\theta_{\mathrm{SP}}\sqrt{1+\mathcal{R}^2\tan^2\theta_{\mathrm{SP}}}}. \tag{2.12}$$

This solution does not immediately look familiar, however, if we recall that $\tilde{n}(\theta_{\mathrm{SP}}) = n_{\mathrm{SP}}(\theta_{\mathrm{SP}})/n_{\mathrm{BG}}$ and rearrange Eq. (2.12) into the form

$$\begin{aligned}\frac{1}{n_{\mathrm{SP}}^2(\theta_{\mathrm{SP}})} &= \frac{\cos^2\theta_{\mathrm{SP}}\left(1+\mathcal{R}^2\tan^2\theta_{\mathrm{SP}}\right)}{n_{\mathrm{BG}}^2\mathcal{R}^2} \\ &= \frac{\cos^2\theta_{\mathrm{SP}}}{n_{\mathrm{BG}}^2\mathcal{R}^2} + \frac{\sin^2\theta_{\mathrm{SP}}}{n_{\mathrm{BG}}^2},\end{aligned} \tag{2.13}$$

we find that it looks similar to an equation that describes the indices of refraction of a uniaxial birefringent crystal. An important aspect of these crystals is the optic axis, which is the direction along which light experiences no birefringence. Light that is not propagating along that direction will be split into two orthogonal polarizations when it passes through the crystal. These polarizations are also orthogonal to the optic axis.

These types of crystals have two indices of refraction. The ordinary index n_{o} is experienced by ordinary rays (o-rays) of light. The extraordinary index $n_{\mathrm{e}}(\vartheta)$ is experienced by extraordinary

rays (e-rays) of light. Uniquely, the extraordinary index of refraction is dependent on the angle ϑ that $\vec{k}$ makes with the optic axis. This phenomenon is used to achieve phase-matching in nonlinear optics. The value of $n_{\mathrm{e}}(\vartheta)$ ranges between n_{o} and the constant n_{e}.

The relationship among all of these parameters is described in Ref. [24] by the equation

$$\frac{1}{n_{\mathrm{e}}^2\left(\vartheta\right)} = \frac{\cos^2\vartheta}{n_{\mathrm{o}}^2} + \frac{\sin^2\vartheta}{n_{\mathrm{e}}^2}. \tag{2.14}$$

Comparing this to Eq. (2.13), we can find the conditions required to make a uniaxial spaceplate. Immediately, we see that only the extraordinary rays will experience the spaceplate effect. Also, in order to get $\theta_{\mathrm{SP}} = \vartheta$, the optic axis must be oriented normal to the interface. This allows us to determine exactly what the extraordinary and ordinary polarizations are, since they are orthogonal to each other and to the optic axis. The e-rays are radially polarized and the o-rays are azimuthally polarized.

Additionally, to get the denominator of the second term of each equation to agree, we need $n_{\mathrm{BG}} = n_{\mathrm{e}}$. Finally, looking at the denominator of the first terms, we find that the compression factor of a uniaxial spaceplate is $\mathcal{R} = n_{\mathrm{o}}/n_{\mathrm{e}} \equiv \mathcal{R}_{\mathrm{e}}$. This final point introduces an additional condition. Since we need $\mathcal{R} > 1$, we therefore need $n_{\mathrm{o}} > n_{\mathrm{e}}$. This describes a negative uniaxial crystal, so named because birefringence is defined as $\Delta n = n_{\mathrm{e}} - n_{\mathrm{o}}$.

So, taking all of these conditions into consideration, the physical system which is described by the $C = 0$ solution is a negative uniaxial crystal whose optic axis is normal to the interface and is surrounded by a background medium with an index of refraction $n_{\mathrm{BG}} = n_{\mathrm{e}}$, wherein only the extraordinary polarization of light will achieve the desired effect. We will learn how the ordinary polarization of light behaves in later derivations.

2.2.3 Limiting Case

Going back once again to the general solution, we can look at the limits of this function to demonstrate the boundaries of our family of solutions. Taking the limit of $\tilde{n}(\theta_{\mathrm{SP}})$ as $\mathcal{R}$ approaches infinity, we find that the boundary of our family of curves is

$$\lim_{\mathcal{R}\to\infty} \tilde{n}(\theta_{\mathrm{SP}}) = \frac{\pm 1}{|\sin\theta_{\mathrm{SP}}|}. \tag{2.15}$$

It is exceedingly unlikely that any physical system could be accurately described by this curve, given the infinitely large compression factor.

2.3 Derivation of Beam Walk-off

Walk-off Δx is a measure of how much a ray of light is laterally displaced as the incident angle increases. It is measured with respect to where the ray forms at $\theta_{\mathrm{BG}} = 0°$.

2.3.1 Low-Index Spaceplate

The walk-off for a low-index spaceplate is easily derived geometrically (Fig. 2.2) using Snell's Law and trigonometry. We begin with a ray of light in the background medium incident on the spaceplate at an angle θ_{BG}. Once the ray is in the spaceplate, it travels at an angle θ_{SP}. We can relate the sines of these angles using Snell's Law,

$$\sin\theta_{\mathrm{SP}} = \frac{n_{\mathrm{BG}}}{n_{\mathrm{SP}}}\sin\theta_{\mathrm{BG}}. \tag{2.16}$$

Recall that θ_{SP} needs to be larger than θ_{BG}, which means that we require $n_{\mathrm{BG}} > n_{\mathrm{SP}}$. The ray reaches the other end of the spaceplate having travelled a distance w in the transverse direction. The beam exits the spaceplate once again propagating at an angle θ_{BG} since the spaceplate has parallel faces. Ultimately, this has resulted in a lateral shift of the beam from its original position. This lateral shift Δx is the walk-off.

Geometrically, we can make a right triangle within the spaceplate where the ray is the hypotenuse, allowing us to use the equation $w = d\tan\theta_{\mathrm{SP}}$, where w is the transverse distance over which the ray has travelled over a distance d in the z direction, the thickness of the spaceplate. For the reference ray (i.e. the ray that would propagate if the spaceplate were not present), we find that the beam would only travel a distance $w_{\mathrm{BG}} = d\tan\theta_{\mathrm{BG}}$ in the transverse direction over a distance d in the z direction. By making a perpendicular line connecting the walked-off beam and the reference beam, we form another right triangle at the exit face of the spaceplate. We

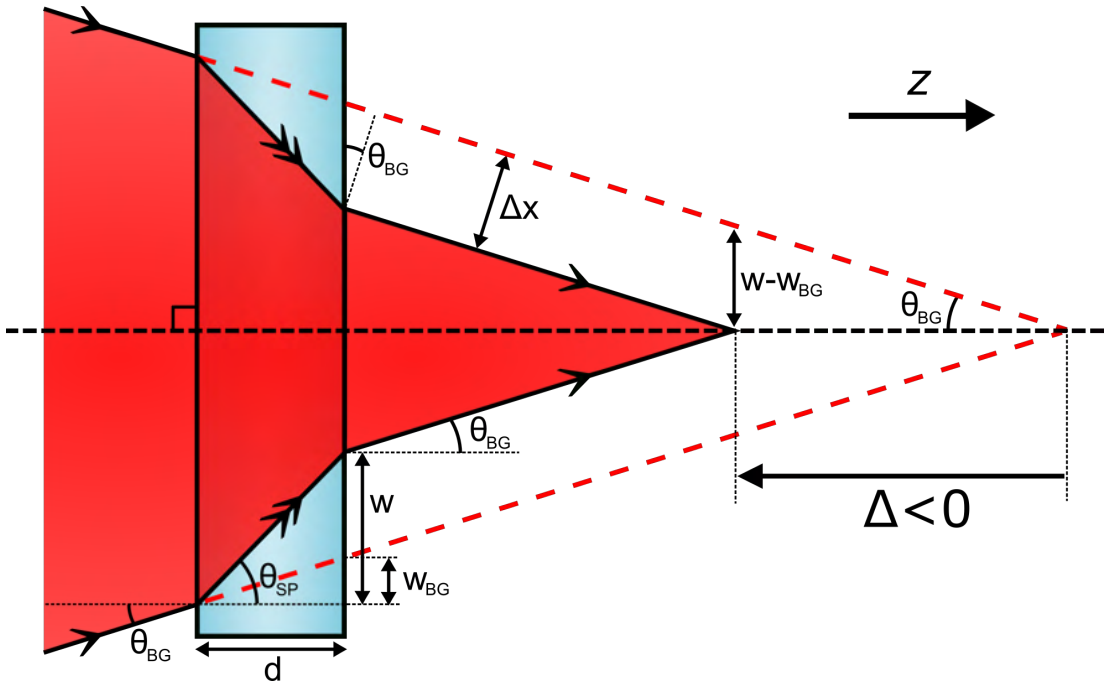

Figure 2.2: A diagram of a beam focussing through a spaceplate, with parameters relevent to the derivations labelled.

can then derive an equation for the walk-off of a low-index spaceplate,

$$\begin{aligned}\Delta x &= (w - w_{\mathrm{BG}})\cos\theta_{\mathrm{BG}} \\ &= d(\tan\theta_{\mathrm{SP}} - \tan\theta_{\mathrm{BG}})\cos\theta_{\mathrm{BG}} \\ &= d(\tan\theta_{\mathrm{SP}}\cos\theta_{\mathrm{BG}} - \sin\theta_{\mathrm{BG}})\,. \end{aligned} \tag{2.17}$$

Using Eq. (2.16) allows us to express the walk-off in terms of just θ_{BG} and not θ_{SP}. Additionally, trigonometric identities will allow us to simplify the equation. The tangent of θ_{SP} can therefore be expressed as

$$\tan\theta_{\mathrm{SP}} = \frac{\sin\theta_{\mathrm{SP}}}{\cos\theta_{\mathrm{SP}}} = \frac{(n_{\mathrm{BG}}/n_{\mathrm{SP}})\sin\theta_{\mathrm{BG}}}{\sqrt{1-(n_{\mathrm{BG}}/n_{\mathrm{SP}})^2\sin^2\theta_{\mathrm{BG}}}} = \frac{\sin\theta_{\mathrm{BG}}}{\sqrt{(n_{\mathrm{SP}}/n_{\mathrm{BG}})^2-\sin^2\theta_{\mathrm{BG}}}}\,. \tag{2.18}$$

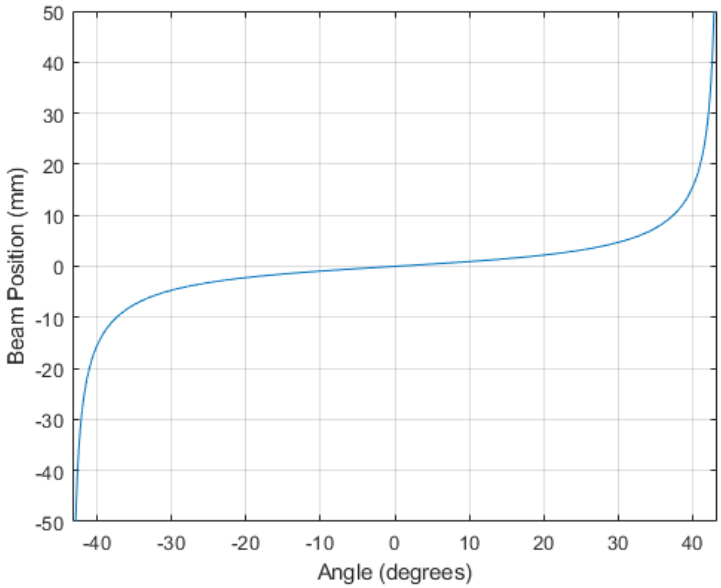

Figure 2.3: Plot of beam walk-off Δx_{LI} as a function of incident angle for a low-index spaceplate. Values for d and the indices of refraction are those described in later chapters for the experimental low-index spaceplate. Note the asymptotes at $\theta_{\mathrm{BG}} = \pm\,\theta_{\mathrm{crit}}$.

Substituting this into Eq. (2.17) results in the equation for the walk-off of a low-index spaceplate,

$$\begin{aligned}\Delta x_{\mathrm{LI}} &= d\left(\frac{\sin\theta_{\mathrm{BG}}\cos\theta_{\mathrm{BG}}}{\sqrt{(n_{\mathrm{SP}}/n_{\mathrm{BG}})^2-\sin^2\theta_{\mathrm{BG}}}}-\sin\theta_{\mathrm{BG}}\right)\\ &= d\sin\theta_{\mathrm{BG}}\left(\frac{\cos\theta_{\mathrm{BG}}}{\sqrt{(n_{\mathrm{SP}}/n_{\mathrm{BG}})^2-\sin^2\theta_{\mathrm{BG}}}}-1\right).\end{aligned} \tag{2.19}$$

Plotting this (Fig. 2.3), we see asymptotes at the critical angle, $\theta_{\mathrm{crit}} = \arcsin(n_{\mathrm{SP}}/n_{\mathrm{BG}})$. This expected result is due to total internal reflection. However, it demonstrates that low-index spaceplates are unsuitable for high NA applications. In addition to limiting the accepted range of angles to the critical angle, this sharp increase in walk-off as a function of angle will also disrupt a focal plane or image plane.

For comparison, we can find what the ideal walk-off for a spaceplate should be. We do this by taking the difference between the walk-off from propagation at an angle θ_{BG} over d_{eff} compared

to that over d. Thus, the ideal walk-off for any spaceplate is

$$\begin{aligned}\Delta x_{\text{ideal}} &= (w - w_{\text{BG}})\cos\theta_{\text{BG}} \\ &= (d_{\text{eff}}\tan\theta_{\text{BG}} - d\tan\theta_{\text{BG}})\cos\theta_{\text{BG}} \\ &= d\left(\frac{d_{\text{eff}}}{d} - 1\right)\tan\theta_{\text{BG}}\cos\theta_{\text{BG}} \\ &= d\sin\theta_{\text{BG}}(\mathcal{R} - 1)\,. \end{aligned} \tag{2.20}$$

We will see that the walk-off of the e-ray through the uniaxial spaceplate better approximates this ideal walk-off.

2.3.2 Uniaxial Spaceplate

Deriving the walk-off due to a uniaxial spaceplate is a bit more difficult. The two different polarizations need to be considered separately. Additionally, we now have to consider that in a birefringent crystal the Poynting vector $\vec{S}$ and the wavevector $\vec{k}$ are not pointed in the same direction. The Poynting vector describes the direction of power flow and is the cross product of the electric and magnetic field vectors. The wavevector describes the propagation direction of the light. Somewhat counter-intuitively, we will need to consider the angle of $\vec{S}$ in the spaceplate, which itself is dependent on the angle of $\vec{k}$ in the spaceplate [25].

For this derivation, which will make extensive use of the information found in Ref. [25], we need to account for the anisotropy of the uniaxial spaceplate. We do this by using the elements of the relative electric permitivity matrix ε_r. Assuming that our media are nonmagnetic ($\mu_r = 1$) and thus using $n = \sqrt{\varepsilon_r\mu_r} = \sqrt{\varepsilon_r}$, we find that the permitivity of a uniaxial spaceplate is

$$\varepsilon_{\text{SP}} = \varepsilon_0\,\varepsilon_r = \varepsilon_0\begin{pmatrix}\varepsilon_{xx} & 0 & \varepsilon_{xz}\\ 0 & \varepsilon_{yy} & 0\\ \varepsilon_{zx} & 0 & \varepsilon_{zz}\end{pmatrix} = \varepsilon_0\begin{pmatrix}n_{\text{o}}^2 & 0 & 0\\ 0 & n_{\text{o}}^2 & 0\\ 0 & 0 & n_{\text{e}}^2\end{pmatrix}. \tag{2.21}$$

The final equality arises due to the orientation of the optic axis, which results in $\varepsilon_{xz} = \varepsilon_{zx} = 0$, $\varepsilon_{xx} = \varepsilon_{yy} = n_{\text{o}}^2$, and $\varepsilon_{zz} = n_{\text{e}}^2$.

We will first derive the walk-off for the e-polarized light, which is the transverse magnetic

(TM) mode, since there is no magnetic field in the direction of propagation for this polarization. Using the notation and equations from Ref. [25], with the exception of changing medium 1 to the background medium (BG), and by substituting in the above values for the elements of the permitivity matrix, we find that the tangent of the angle of $\vec{k}$ is

$$\begin{aligned}\tan\theta_{2k}^{\mathrm{TM}} &= \frac{\varepsilon_{zz}\sin\theta_{\mathrm{BG}}}{-\varepsilon_{xz}\sin\theta_{\mathrm{BG}} + \sqrt{\left(\varepsilon_{xx}\varepsilon_{zz}-\varepsilon_{xz}^2\right)\left(\varepsilon_{zz}/\varepsilon_{\mathrm{BG}}-\sin^2\theta_{\mathrm{BG}}\right)}} \\ &= \frac{(n_{\mathrm{e}}/n_{\mathrm{o}})\sin\theta_{\mathrm{BG}}}{\sqrt{(n_{\mathrm{e}}/n_{\mathrm{BG}})^2-\sin^2\theta_{\mathrm{BG}}}}\,. \end{aligned} \tag{2.22}$$

We than can substitute this into the expression for the tangent of the angle of $\vec{S}$,

$$\begin{aligned}\tan\theta_{2S}^{\mathrm{TM}} &= \frac{\varepsilon_{xz}+\varepsilon_{xx}\tan\theta_{2k}^{\mathrm{TM}}}{\varepsilon_{zz}+\varepsilon_{xz}\tan\theta_{2k}^{\mathrm{TM}}} \\ &= \frac{(n_{\mathrm{o}}/n_{\mathrm{e}})\sin\theta_{\mathrm{BG}}}{\sqrt{(n_{\mathrm{e}}/n_{\mathrm{BG}})^2-\sin^2\theta_{\mathrm{BG}}}}\,. \end{aligned} \tag{2.23}$$

Note the change in the ratio of indices in the numerator. From here, the derivation is the same as that for the low-index spaceplate, using $\tan\theta_{2S}^{\mathrm{TM}}$ as $\tan\theta_{\mathrm{SP}}$ in Eq. (2.17). The final equation for the walk-off of an extraordinary ray is

$$\Delta x_{\mathrm{e}} = d\sin\theta_{\mathrm{BG}}\left(\frac{(n_{\mathrm{o}}/n_{\mathrm{e}})\cos\theta_{\mathrm{BG}}}{\sqrt{(n_{\mathrm{e}}/n_{\mathrm{BG}})^2-\sin^2\theta_{\mathrm{BG}}}}-1\right). \tag{2.24}$$

Similarly, the equation for the walk-off of an ordinary ray is

$$\Delta x_{\mathrm{o}} = d\sin\theta_{\mathrm{BG}}\left(\frac{\cos\theta_{\mathrm{BG}}}{\sqrt{(n_{\mathrm{o}}/n_{\mathrm{BG}})^2-\sin^2\theta_{\mathrm{BG}}}}-1\right). \tag{2.25}$$

These two equations appear similar, but plotting them (Fig. 2.4) reveals some key differences. First, at low incident angles, the walk-off occurs in opposite directions for these two polarizations. Once Δx_{e} reaches a particular angle, it changes direction. Additionally, the two beams become one again at $\theta_{\mathrm{BG}} = \pm 90°$.

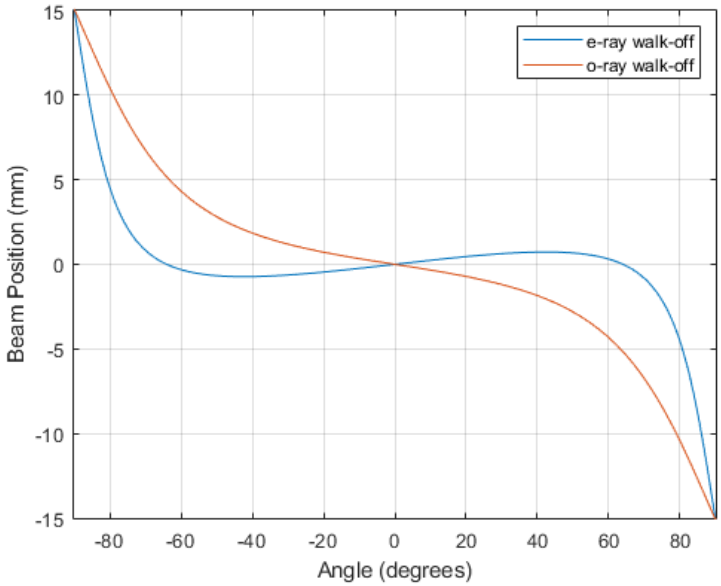

Figure 2.4: Plot of beam walk-offs Δx_e and Δx_o as a function of incident angle for a uniaxial spaceplate. Values for d and the indices of refraction are those described in later chapters for the experimental uniaxial spaceplate. Note the change in direction for the e-polarized beam.

2.4 Derivation of Beam Waist Shift

To determine how much the waist of a focusing beam is shifted in the negative z direction with the addition of a spaceplate to an optical system, we will need to use a few of the equations derived in the previous section. First, let's take the system of light rays focusing through a spaceplate. The light comes to a focus, forming the beam waist at a point in the background medium after exiting the spaceplate. If the spaceplate were not there, the beam waist would have focused at a more distant point. These two points are separated by a distance Δ. We define this shift in the beam waist to be negative, since the beam waist moves in the negative z direction when a spaceplate is added to a system.

Using values defined in the walk-off derivation, as well as basic trigonometry, we get an equation for the beam waist shift,

$$\Delta = \frac{-(w - w_\mathrm{BG})}{\tan\theta_\mathrm{BG}}, \tag{2.26}$$

where the factor of -1 comes from our definition of Δ. We can then use the definitions of w and w_{BG} to rewrite the beam waist shift as

$$\Delta = \frac{d(\tan\theta_{\mathrm{BG}} - \tan\theta_{\mathrm{SP}})}{\tan\theta_{\mathrm{BG}}} = d\left(1 - \frac{\tan\theta_{\mathrm{SP}}}{\tan\theta_{\mathrm{BG}}}\right). \tag{2.27}$$

For the low-index spaceplate, we use Eq. (2.18) to get an exact equation for beam waist shift,

$$\begin{aligned}\Delta_{\mathrm{LI}} &= d\left(1 - \frac{\sin\theta_{\mathrm{BG}}}{\tan\theta_{\mathrm{BG}}\sqrt{(n_{\mathrm{SP}}/n_{\mathrm{BG}})^2 - \sin^2\theta_{\mathrm{BG}}}}\right) \\ &= d\left(1 - \frac{\cos\theta_{\mathrm{BG}}}{\sqrt{(n_{\mathrm{SP}}/n_{\mathrm{BG}})^2 - \sin^2\theta_{\mathrm{BG}}}}\right).\end{aligned} \tag{2.28}$$

Plotting this equation (Fig. 2.5), we see that the asymptote at the critical angle remains. Additionally, at small angles, this shift is approximately constant. So, for small angles, our equation can be approximated as

$$\Delta_{\mathrm{LI}} \approx d\left(1 - \frac{n_{\mathrm{BG}}}{n_{\mathrm{SP}}}\right) = d(1 - \mathcal{R}_{\mathrm{LI}}), \tag{2.29}$$

which gives us our definition of $\mathcal{R}_{\mathrm{LI}}$. We will verify this experimentally.

For the uniaxial spaceplate, we will have two equations for beam waist shift. One for the e-polarized beam and one for the o-polarized beam. In the case of e-polarized light, we will use Eq. (2.23) in place of $\tan\theta_{\mathrm{SP}}$. This results in a shift of

$$\Delta_{\mathrm{e}} = d\left(1 - \frac{(n_{\mathrm{o}}/n_{\mathrm{e}})\cos\theta_{\mathrm{BG}}}{\sqrt{(n_{\mathrm{e}}/n_{\mathrm{BG}})^2 - \sin^2\theta_{\mathrm{BG}}}}\right) \approx d\left(1 - \frac{n_{\mathrm{o}}n_{\mathrm{BG}}}{n_{\mathrm{e}}^2}\right) = d(1 - \mathcal{R}_{\mathrm{e}}). \tag{2.30}$$

This new definition of $\mathcal{R}_{\mathrm{e}}$ gives a more complete picture of the system, because it considers $n_{\mathrm{BG}} \neq n_{\mathrm{e}}$. This can alternatively be called a "mixed spaceplate" since it incorporates aspects of both the uniaxial and low-index spaceplates.

The o-polarized beam waist will experience a shift in the opposite direction (positive z) and thus we will see that $0 < \mathcal{R}_{\mathrm{o}} < 1$ and the value of Δ_{o} is positive. Through a similar derivation,

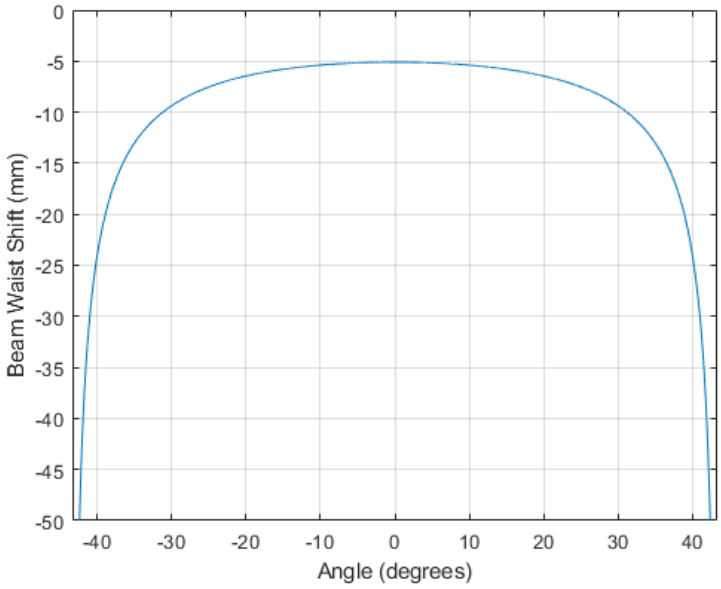

Figure 2.5: Plot of beam shift Δ_{LI} as a function of incident angle for a low-index spaceplate. Values for d and the indices of refraction are those described in later chapters for the experimental low-index spaceplate.

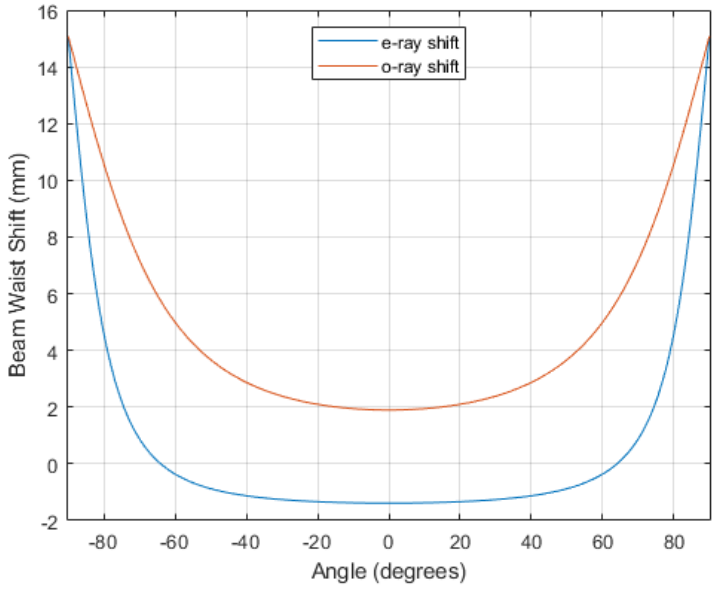

Figure 2.6: Plot of beam shifts Δ_{e} and Δ_{o} as a function of incident angle for a uniaxial spaceplate. Values for d and the indices of refraction are those described in later chapters for the experimental uniaxial spaceplate.

we find that the beam waist shift for an ordinary polarized beam is

$$\Delta_{\mathrm{o}} = d\left(1 - \frac{\cos\theta_{\mathrm{BG}}}{\sqrt{(n_{\mathrm{o}}/n_{\mathrm{BG}})^2 - \sin^2\theta_{\mathrm{BG}}}}\right) \approx d\left(1 - \frac{n_{\mathrm{BG}}}{n_{\mathrm{o}}}\right) = d(1 - \mathcal{R}_{\mathrm{o}})\,. \tag{2.31}$$

The angle-dependent equations of both Δ_{e} and Δ_{o} are plotted in Fig. 2.6. Notice that Δ_{e} is negative until large angles, but both shifts are approximately constant at low angles. We will compare the values calculated from the simplified equations to the measured values of beam waist shift.

Lastly, let's take this generalized equation for beam waist shift, $\Delta = d(1-\mathcal{R})$, and reintroduce our original definition for the compression factor. From this we see that

$$\Delta = d\left(1 - \frac{d_{\mathrm{eff}}}{d}\right) = d - d_{\mathrm{eff}}\,. \tag{2.32}$$

This demonstrates that the beam waist shift Δ is an accurate demonstration of how much propagation distance has been reduced.

2.5 Chromatic Aberration

For the sake of simplicity, we will only be considering longitudinal chromatic aberration. In particular, we want to see how Δ changes with wavelength. This will serve as a measure of the dispersion in a spaceplate. To find this, we need to know how the index of refraction changes with wavelength. Unfortunately, there are only empirical solutions for this, which are fit to experimental data, such as Sellmeier equations or Cauchy's transmission equations. Those equations can be substituted into the following equations to find the dispersion of a given spaceplate.

For low-index spaceplates, the change in shift with repect to wavelength is

$$\begin{aligned}\frac{\partial\Delta_{\mathrm{LI}}}{\partial\lambda} &= d\,\frac{\partial}{\partial\lambda}\left[1 - \frac{n_{\mathrm{BG}}(\lambda)}{n_{\mathrm{SP}}(\lambda)}\right] \\ &= \frac{d}{n_{\mathrm{SP}}^2(\lambda)}\left[n_{\mathrm{BG}}(\lambda)\frac{\partial\, n_{\mathrm{SP}}(\lambda)}{\partial\lambda} - n_{\mathrm{SP}}(\lambda)\frac{\partial\, n_{\mathrm{BG}}(\lambda)}{\partial\lambda}\right].\end{aligned} \tag{2.33}$$

For the e-polarization of the uniaxial spaceplate, using our new $\mathcal{R}_{\mathrm{e}}$, we find

$$\begin{aligned}\frac{\partial \Delta_{\mathrm{e}}}{\partial \lambda} &= d\,\frac{\partial}{\partial \lambda}\left[1-\frac{n_{\mathrm{o}}(\lambda)\,n_{\mathrm{BG}}(\lambda)}{n_{\mathrm{e}}^2(\lambda)}\right] \\ &= \frac{-\,d}{n_{\mathrm{e}}^3(\lambda)}\left[n_{\mathrm{BG}}(\lambda)\,n_{\mathrm{e}}(\lambda)\frac{\partial\, n_{\mathrm{o}}(\lambda)}{\partial \lambda}+n_{\mathrm{o}}(\lambda)\,n_{\mathrm{e}}(\lambda)\frac{\partial\, n_{\mathrm{BG}}(\lambda)}{\partial \lambda}-2\,n_{\mathrm{o}}(\lambda)\,n_{\mathrm{BG}}(\lambda)\frac{\partial\, n_{\mathrm{e}}(\lambda)}{\partial \lambda}\right]. \quad (2.34)\end{aligned}$$

Lastly, the equation for o-polarized light through a uniaxial spaceplate is

$$\begin{aligned}\frac{\partial \Delta_{\mathrm{o}}}{\partial \lambda} &= d\,\frac{\partial}{\partial \lambda}\left[1-\frac{n_{\mathrm{BG}}(\lambda)}{n_{\mathrm{o}}(\lambda)}\right] \\ &= \frac{d}{n_{\mathrm{o}}^2(\lambda)}\left[n_{\mathrm{BG}}(\lambda)\frac{\partial\, n_{\mathrm{o}}(\lambda)}{\partial \lambda}-n_{\mathrm{o}}(\lambda)\frac{\partial\, n_{\mathrm{BG}}(\lambda)}{\partial \lambda}\right]. \quad (2.35)\end{aligned}$$

We want to minimize all of these derivatives to minimize the chromatic aberration of the spaceplates. However, if there is a spaceplate which demonstrates an unacceptable amount of longitudinal chromatic aberration, this can largely be reduced by corrective lenses or lens systems. Unfortunately, we have not yet taken measurements to validate these equations. This will be left for future work.

Chapter 3

Methods for Characterizing the Performance of Spaceplates

In this chapter, I will present the experimental methods used in order to verify our theory. The results using these methods will be presented in Chapters 4 and 5 for a low-index spaceplate and a uniaxial spaceplate, respectively.

3.1 Experimental Setups

There were two similar setups used in our measurements. One was the beam setup and the other was the imaging setup. Rather than describing both in detail, to avoid repetition, I will describe the beam setup in detail, then state how the imaging setup was modified.

3.1.1 Beam Setup

The beam setup (Fig. 3.1) begins with the light source, which is a 4.5 mW continuous wave laser that emits 532 nm wavelength light. This is followed by a neutral density filter which reduced the intensity of the beam. This is followed by a shutter which can block the beam. Then, we have a 4f system which reduces the width of the beam. A 4f system is a pair of lenses separated by the sum of their focal lengths which has the effect of changing the diameter of the beam. The magnification of a 4f system is given by $M = -f_2/f_1$, where f_1 is the focal length of the first lens and f_2 is the focal length of the second lens. Since the beam is collimated when it enters the 4f system, it is also collimated at the output.

The purpose of reducing the beam diameter here is so that the beam can be completely

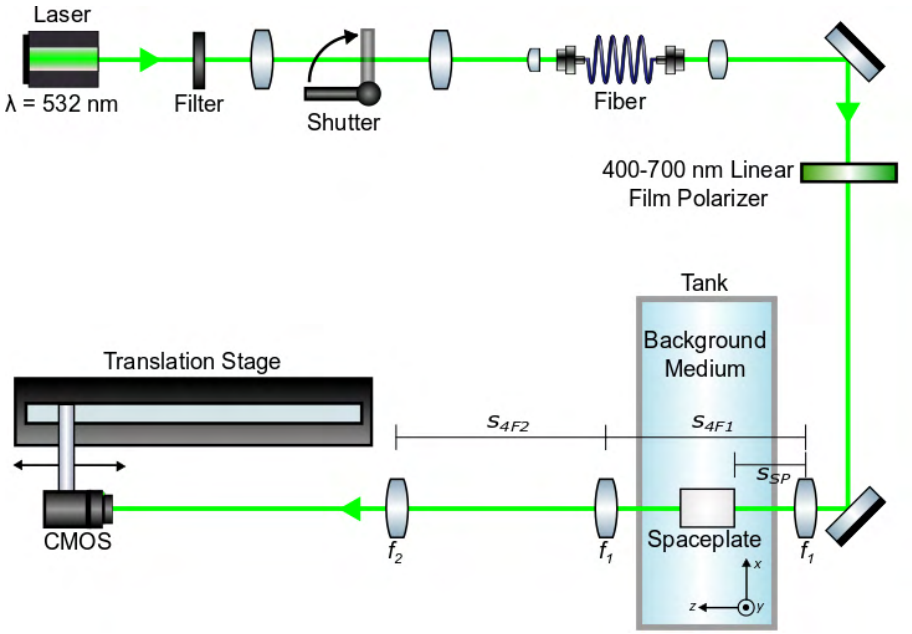

Figure 3.1: Diagram of the beam setup.

incident on the small aspheric lens which couples the beam into a single-mode fiber optic. This fiber ensures that the beam consists of only the fundamental (lowest-order) Gaussian mode. After exiting the fiber, the beam is then collimated by a microscope objective lens. At this point in the system, the collimated beam is about 3.8 mm in diameter, using the $1/e^2$ intensity definition.

We then have a broadband (400 nm − 700 nm) film polarizer, which renders the beam linearly polarized. Rotating this polarizer allows us to change the angle of the linear polarization. This polarizer is only used when the uniaxial spaceplate is present, since that is the only system that we test which is polarization-dependent.

The beam then goes through a lens whose focal length is $f_1 = 10$ cm, which focuses the light into a rectangular glass tank. The glass has a thickness of (4.9 ± 0.1) mm and the width of the tank is (100.8 ± 0.1) mm, including the thickness of the glass. This tank is filled with the liquid background medium, glycerol. Previously, the background medium was flaxseed oil (a.k.a. linseed oil), which better matches the extraordinary index of the uniaxial spaceplate that we use. We changed it to glycerol so that more of the visible spectrum of light would be transmitted. Glycerol has over 95% transmittance for the entire visible spectrum [26], while flaxseed oil has

extremely low transmittance at visible wavelengths less than about 500 nm.

The spaceplate being tested can be inserted into the background medium in the path of the beam. It is mounted on a rotation stage, which allows for rotation about the y axis. It is placed at a distance $s_{\mathrm{SP}} \approx 8$ cm, but this value can vary by as much as a few centimetres. Note that the exact position of the spaceplate along the path of the light does not affect its performance.

The NA of this beam setup is determined by the angle of focusing light rays approaching the spaceplate. First, we take the width (radius) of our beam, which is 1.9 mm, and send it through our 10 cm lens. Since the incoming beam is collimated prior to the lens, the beam waist would form 10 cm away from the lens (if the tank were not present). Using trigonometry, we determine that the angle of light approaching the tank is $\theta = 1.088°$. Using $\mathrm{NA} = n \sin\theta$, we find that NA=0.019 for this setup.

There is another $f_1 = 10$ cm focal length lens on the opposite side of the tank which forms a 4f system with the first f_1 lens (i.e. $s_{4\mathrm{F1}} = 20$ cm). This second lens also forms another 4f system with either an $f_2 = 20$ cm or $f_2 = 25$ cm lens, depending on the measurement, which serves to magnify the beam, as well as increase the walk-off and beam waist shift. This makes $s_{4\mathrm{F2}} = 30$ cm or 35 cm.

Lastly, there is a CMOS colour light sensor mounted on a translation stage oriented along the z axis, whose minimum step size is 0.01 inch (0.254 mm). It has a resolution of 1936 px $\times$ 1216 px, where each pixel has an area of 5.86 μm $\times$ 5.86 μm. The total area of the detector is 11.345 mm $\times$ 7.126 mm. The shutter, translation stage, and CMOS sensor are all controlled automatically by our LabView software, into which we enter the base file name for the raw data, the step size for the translation stage, the total number of steps, the number pictures taken at each step, and the exposure time of the CMOS sensor.

3.1.2 Imaging Setup

Much of this setup is similar to the beam setup, but with a few key differences. Rather than restating all of the similarities, I will describe how this setup differs from the beam setup. Furthermore, it is illustrated in its entirety in Fig. 3.2. Firstly, everything prior to the film polarizer is removed, except for the shutter. Instead, we have an incoherent white light source

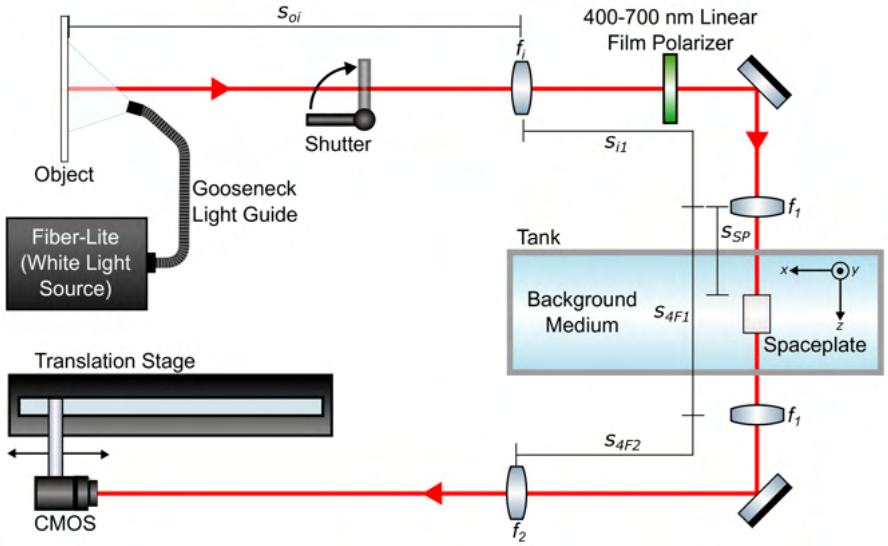

Figure 3.2: Diagram of the imaging setup.

Figure 3.3: **(a)** The original painting "War Canoes, Alert Bay" by Emily Carr. **(b)** The colour saturated version used as our object. **(c)** The physical print as imaged through our imaging system, in the case of free space propagation (i.e. no tank or spaceplate present).

which illuminates the object.

Our object is a modified print of the painting "War Canoes, Alert Bay" by Emily Carr, 1912 (Fig. 3.3.a). We saturated the colours (Fig. 3.3.b) in order to better retain them after the image goes through the background medium. The dimensions of the print were (8.0 ± 0.5) mm $\times$ (6.5 ± 0.5) mm. At this size, and given the overall magnification of the system, we were able to distinguish the individual printing dots of the object (Fig. 3.3.c).

Also, to better collect light reflected off of the object, we inserted a 25 cm focal length lens with a diameter of 2 inches (5.08 cm). It was positioned at a distance of about $s_{\text{oi}} = 11$ cm in

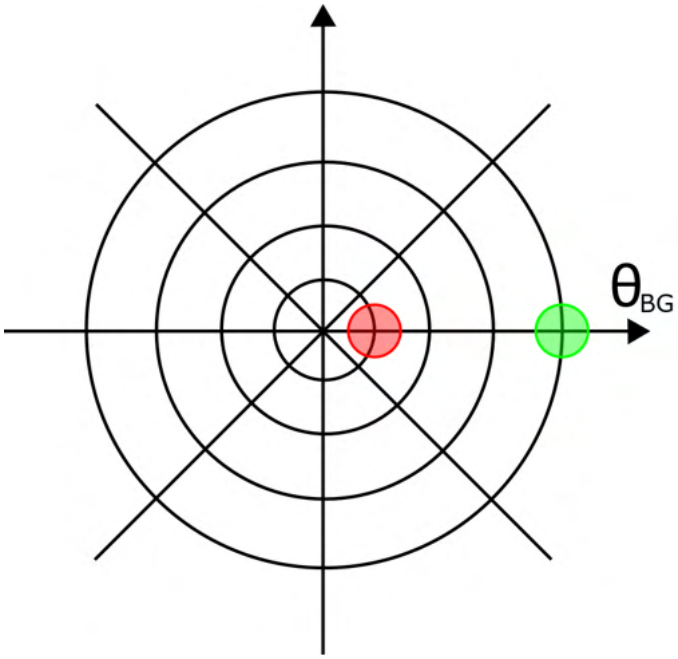

Figure 3.4: Diagram depicting radial and azimuthal polarizations of light. The red circle depicts the range of angles incident on a uniaxial spaceplate at low tilt about the y axis. The green circle depicts the range of incident angles at higher tilt.

front of the object and roughly $s_{i1} = 35$ cm behind the 10 cm lens. The only other difference is that, in this setup, we strictly use the $f_2 = 20$ cm lens as the final lens in the system.

Unlike in the beam setup, this last lens determines the NA of this system. To determine the numerical aperture in this case, we can use NA $\approx D/(2f)$, where D is the diameter of the lens. Since this lens has a diameter of 1 inch (2.54 cm), we find that NA=0.0635, which corresponds to $\theta = 3.64°$. For context, a good cell phone camera has NA=0.277 (or $\theta = 16°$).

3.1.3 Isolating the Polarizations for the Uniaxial Spaceplate

Special considerations must be made in performing these measurements with the uniaxial spaceplate, given its polarization-dependence. Since the uniaxial spaceplate separates light into radial and azimuthal polarizations, it would be difficult to prepare these individual polarizations. What we do instead is linearly polarize the light, which can approximate either radial or azimuthal at sufficiently large incident angles.

As incident angles close to zero (the red circle in Fig. 3.4), it is clear that linear polarizations

are very different from radial and azimuthal. However, as incident angle increases, they become increasingly similar. In our measurements, we increase incident angle by tilting the uniaxial spaceplate about the vertical y axis. At this larger angle in the x-z plane (the green circle in Fig. 3.4), we observe that radial polarization is approximately linear horizontal polarization, while azimuthal is approximately linear vertical.

From this, we know that setting the linear polarization to horizontal will isolate the e-polarized light (which experiences the desired spaceplate effect) and setting it to vertical will isolate the o-polarized light (which does not experience the desired effect). The minimum spaceplate tilt angle required to isolate a polarization is dependent on the intensity of the light and the range of angles incident on the spaceplate. In particular, the beam setup generally requires a smaller angle than the imaging setup, since the imaging setup has a larger NA.

3.2 Types of Measurements Taken

We have taken a few different types of measurements for this experiment. The first two used the beam setup, while the last one used the imaging setup.

3.2.1 Beam Waist Shift

This is the main measurement that we use to provide evidence for the spaceplate effect. For this type of measurement, we take a background measurement (i.e. with the shutter closed, blocking the beam) using the CMOS sensor. Then, with the beam present, the CMOS sensor is translated incrementally along the z axis, taking a picture at each step. From this, we are able to determine where the beam waist forms, and therefore, we can see the Δ in the beam waist after a change to the system, such as adding a spaceplate.

Given that we are working with an approximately Gaussian beam, the width (radius) of the beam is described by

$$W(z) = W_0 \sqrt{1 + \left(\frac{z}{z_R}\right)^2}, \tag{3.1}$$

where W_0 is the width of the beam waist (located at $z = 0$) and $z_R = \pi W_0^2 n/\lambda$ is the Rayleigh

range. The Rayleigh range is the distance between $z = 0$ and the position at which $W = \sqrt{2}\,W_0$. For this reason, the depth of focus is equal to twice the Rayleigh range. This equation describes the ideal case, however, imperfections in the optics and aberrations make this equation less useful.

The equations that will be used in the analysis of the beam shift are Eq. (2.29), Eq. (2.30), and Eq. (2.31), which were derived in the previous chapter. However, given our setup, we now need to consider both the change in medium and the magnification of the last 4f system. Doing so allows us to relate the shift in the tank Δ to the shift at the CMOS sensor on the translation stage,

$$\Delta^{\mathrm{CMOS}} = \frac{\Delta}{n_{\mathrm{BG}}} \left(\frac{f_2}{f_1}\right)^2 . \tag{3.2}$$

The factor being multiplied with Δ is the longitudinal magnification of our system. The last lens in our beam setup, for this type of measurement, has a focal length of $f_2 = 25$ cm.

To make the plots for this type of measurement, we take the images captured by the CMOS detector at each step, and we integrate those images along one direction. Those compressed images are placed sequentially such that it resembles the converging beam viewed from the side. In other words, we are plotting the beam profile. This makes it easy to determine the position at which the beam waist forms by finding the circle of least confusion.

3.2.2 Beam Walk-off

For this type of measurement, we keep the CMOS sensor stationary as we increase the incident angle of the light incrementally. This is done by rotating the spaceplate about the vertical axis via the rotation stage. This, in effect, increases the angle of incidence of the incoming light. After exiting the spaceplate, the beam has been laterally displaced by a distance Δx, which is the angle-dependent walk-off. On the sensor, we observe a beam spot which translates as function of θ_{BG}.

The change from background medium to free space does not significantly affect the lateral displacement of the beam. However, we still need to consider how the 4f system affects the it. To find the theoretical equation for walk-off at the CMOS sensor, we simply take Eq. (2.19), Eq. (2.24), or Eq. (2.25) and introduce a factor of $M = -f_2/f_1$, the transverse magnification of

a 4f system, which can be confirmed by a ray diagram. For this reason, we use the $f_2 = 20$ cm lens as the final lens for this type of measurement. This allows us to keep the beam incident on the CMOS sensor for larger angles. Similarly, we've used thinner spaceplates than the ones we used in Ref. [19] in order to achieve a larger range for this type of measurement. However, this may have adversely affected the accuracy of the shift measurements.

An important aspect of the walk-off measurement is that it allows us to check for potential aberrations at high incident angles. By increasing the incident angle, we are essentially probing higher NA values. If the measured walk-off were to differ significantly from the theory, especially at higher angles, we would know that aberrations are present in the system.

Our plots for this type of measurement are made using the same method as the beam waist shift plots. But, for these plots, we will superimpose the theoretical walk-off, adjusted such that it describes the walk-off at the CMOS sensor. In practice, this simply means introducing a factor of two, since $|M| = f_2/f_1 = 2$ for this type of measurement. We also translate the theory curve such that its first point is at the same position as the first experimental data point.

3.2.3 Image Shift

This type of measurement is very similar to the beam waist shift measurement. However, there are additional complications. Firstly, since we are using an image, rather than a laser beam, it is more difficult to determine the exact location of the image plane. Previously, we simply had to determine where the beam width was smallest. Now, we can only subjectively determine where the image looks most "in focus." This is further complicated by the imaging setup's relatively large depth of field, the range over which the image appears to be in focus. This depth of field will determine the uncertainty of these measurements. Additionally, the image plane is not perfectly flat, thereby further confusing its exact position. This means that different parts of the image can are focused at slightly different z positions. However, this will not be a significant issue, because the curvature is sufficiently small and every part of the image plane is located well within our uncertainty range, the depth of field.

In practical terms, the way we determine the position of the image plane is by looking at the sharpness of the image at each position. In particular, I look at the printing dots, the texture of

the paper, and the sections of colour in the image. The depth of field is determined subjectively by observing at which position the image becomes blurry. This also helps to inform where the image plane is located, since it should be roughly in the middle of the depth of field.

Since the NA of the imaging system is not significantly larger than that of the beam system, we can continue to use the low angle approximation used to simplify the theoretical equation for shift to $\Delta = d(1 - \mathcal{R})$, rather than the more accurate angle-dependent version. Since the last lens in the imaging setup has $f_2 = 20$ cm, we'll need to use that in our application of Eq. (3.2) when calculating the theoretical values of shift.

It is not feasible to make a plot for these measurements in a similar style to the previous ones, so we will simply display the raw data at positions of interest. Namely, the locations of the image plane for each of the systems. The main purpose of showing these images is to demonstrate how the addition of the spaceplate affects the quality of the images in comparison to the the image through just glycerol. In particular, does the spaceplate cause any aberrations?

Chapter 4

Experimental Demonstration of a Low-Index Spaceplate

4.1 Measuring the Index of Refraction of the Glycerol

Our background medium is glycerol with a purity $\geq 99.5\%$, as stated by the manufacturer. Assuming that this given value of purity is correct, the index of refraction would be $n_{\mathrm{BG}} = 1.473$, approximately [27]. This index of refraction is measured at the wavelength of 589 nm, which is one of the D-lines in the sodium emission spectrum.

However, using our own MA871 refractometer, we find a slightly different value for the index. This refractometer was designed to determine the brix percentage, which is a measure of a liquid's sucrose concentration by weight. It does this by using a prism and applying the concept of critical angles to find the index of refraction for the liquid. It then automatically converts that into the brix percentage. We will simply take the brix measurement and convert it back into the index of refraction.

The measured brix percentage was $(63.9 \pm 0.2)\%$, which corresponds to a refractive index of $n_{\mathrm{BG}} = 1.45090 \pm 0.00047$ based on the conversion table by the International Commission for Uniform Methods of Sugar Analysis [28]. The values in this table are measured using 589 nm light and at a temperature of 20°C. The measured temperature in our lab was 23.3°C and we want the index of refraction for the wavelength of our laser, 532 nm. Thankfully, our refractometer already compensates for the difference in temperature.

But we still need to consider how much the index of refraction differs between 589 nm light

Figure 4.1: Photo of the airplate, our low-index spaceplate used in experiments.

and 532 nm light. Looking at the data from Ref. [29], we determine that the index of refraction at 532 nm is larger than that at 589 nm by 0.0028. Therefore, we can add that same difference to our measured index of refraction and round up our uncertainty, giving us $n_{\mathrm{BG}} = 1.4537 \pm 0.0005$, which we will use in all of our calculations.

4.2 Design and Fabrication of Airplate

Since this type of spaceplate has of compression factor of $\mathcal{R}_{\mathrm{LI}} = n_{\mathrm{BG}}/n_{\mathrm{SP}}$, the best possible spaceplate that can be reasonably fabricated is one that consists of air. This would simplify the compression factor to $\mathcal{R}_{\mathrm{LI}} = n_{\mathrm{BG}}$. Again, this means that this spaceplate cannot work in free space. It is as a proof of concept which reduces the light propagation along z within the background medium.

To make this low-index spaceplate, we made a rudimentary air cell out of a 1 inch diameter lens tube with microscope cover slips adhered to either end using epoxy. We refer to this as an "airplate" (Fig. 4.1). The glass cover slips ranged in thickness from 0.13 mm to 0.16 mm. These airplates were capable of being submerged without the glycerol background medium leaking in.

The airplate had a thickness of $d = (11.26 \pm 0.06)$ mm, including the thickness of the glass. This was determined by taking the mean of 14 caliper measurements of the airplate's thickness and the uncertainty is the standard error of that data set. The airplate was thick enough to demonstrate a shift of the beam waist or image plane, but thin enough to be used for the walk-off measurements to obtain a large range of values for incident angle.

4.3 Beam Waist Shift

As previously mentioned, the airplate must be submerged in a background medium with a higher index of refraction. Thinking about Snell's Law, there is no way for there to be better performance of the airplate in high-index background compared to propagation in only air. These experiments are proofs of concept; they demonstrate the function of a spaceplate. While this demonstration may be trivial, these ideas can be applied to other cases where there would be a net improvement over free space propagation. These will be discussed in the Conclusion chapter.

First, we perform a beam waist shift measurement without the background medium or the spaceplate present. This is our free space propagation. It is included for completeness, but it is not relevant for the proof of concept. We see that the beam comes to a focus at a position along the z axis (Fig. 4.2.a). The beam's smallest width is the beam waist. We will observe how the beam waist shifts along z with the addition of the glycerol background medium, then with the airplate. Our smallest increment (a.k.a. the step size) in these beam shift measurements is 0.04 inches (0.1 cm), which will be our uncertainty.

With the addition of the glycerol, the beam waist shifts in the positive z direction (Fig. 4.2.b), given that the beam is now propagating through approximately 10 cm of this higher index (HI) medium. The beam shift is measured to be $\Delta_{\mathrm{HI}}^{\mathrm{CMOS}} = (+20.0 \pm 0.1)$ cm along the translation stage, using the CMOS sensor. This tank of glycerol can be viewed as a "high-index" spaceplate, much like the glass plate mentioned in the first chapter, with $d = (10.08 \pm 0.01)$ cm and $0 < \mathcal{R} < 1$. Specifically, $\mathcal{R}_{\mathrm{HI}} = 1/n_{\mathrm{BG}} = 0.6879$, which gives us a theoretical shift of $\Delta_{\mathrm{HI}}^{\mathrm{CMOS}} = +19.66$ cm at the translation stage, calculated using Eq. (3.2) and $\Delta_{\mathrm{HI}} = d\,(1 - \mathcal{R}_{\mathrm{HI}})$, modified from Eq. (2.29). Note that we applied Eq. (3.2) because the theoretical value of shift needs to be converted to that observed by the CMOS sensor at the translation stage, after the 4f system. For the high-index

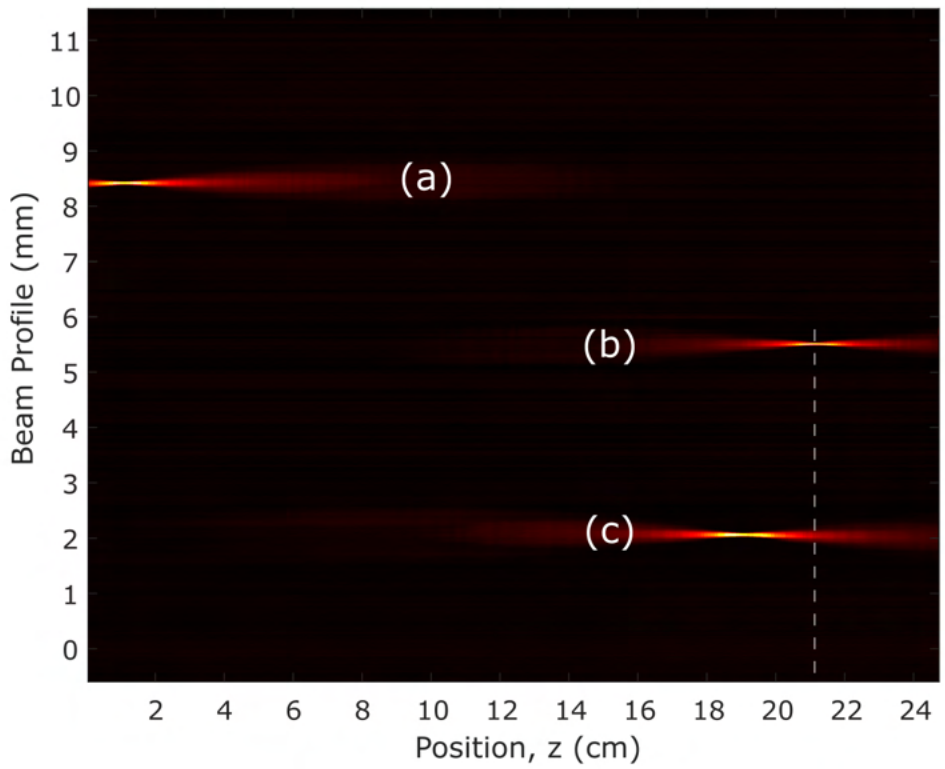

Figure 4.2: Experimental data depicting the profile of a beam through **(a)** only free space, **(b)** glycerol, and **(c)** airplate in glycerol. The data from each trial has been superimposed into this figure and each beam's placement along the vertical axis is arbitrary. This depicts the beam profile at the translation stage, not the beam profile in the tank. The white dashed line denotes the position of the beam waist through glycerol. Note that all of the beam plots use false colour. The more yellow/white data points depict a higher intensity.

shift values only, we set $n_{\mathrm{BG}} = 1$, since they are shifting with respect to free space. For all other shift values, we use the index of glycerol, since they are shifting with respect to the glycerol background medium.

Comparing the experimental value to the theoretical value of the shift due to the high-index medium, we see that the theoretical value is not quite within the uncertainty range of the experimental value. However, they are equivalent when rounded to the nearest centimetre. Furthermore, there is only a percent error of 1.78 %, which is reasonably low.

Adding our airplate to the system shifts the beam waist in the desired negative z direction by $\Delta_{\mathrm{LI}}^{\mathrm{CMOS}} = (-2.0 \pm 0.1)$ cm at the translation stage (Fig. 4.2.c). The theoretical shift is

$\Delta_{\mathrm{LI}}^{\mathrm{CMOS}} = -2.1906$ cm. Again, this is not quite within the range of uncertainty. Unfortunately, the percent error of 8.70 % is quite a bit larger for this measurement than it was for the previous one.

All of the above experimental values for shift were found using data that was taken at the translation stage, after the last 4f system, in free space. But this does not accurately reflect the amount of propagation distance that has been reduced by the airplate. Instead, these values should be converted, using Eq. 3.2, to the shift that occurs in the tank, prior to the final 4f lens system. The converted values for all beam shifts and image shifts are listed in Table 6.1, including the predicted value for these shifts. Since these conversions only involve multiplication, the percent errors found still apply to the converted values.

For the high-index shift, we have an experimental value of $\Delta_{\mathrm{HI}} = (+3.20 \pm 0.02)$ cm at the tank, compared to a predicted value of $\Delta_{\mathrm{HI}} = 3.146$ cm. With the introduction of the airplate, the beam waist shifts by $\Delta_{\mathrm{LI}} = (-0.47 \pm 0.02)$ cm, compared to the predicted $\Delta_{\mathrm{LI}} = -0.5095$ cm.

4.4 Beam Walk-off

With our airplate in glycerol system, we start with zero degrees tilt and increment by 0.5°, taking a photo of the beam at each step. The CMOS detector remains stationary at an arbitrary position near the beam waist. This is acceptable because the lateral position of the beam does not change along the z direction for a given value of spaceplate tilt.

Theoretically, the walk-off reaches an asymptote at the critical angle. For our airplate, $\theta_{\mathrm{crit}} = 43.6°$. The range of data we took was from 0° to 33.5°, as depicted in Fig. 4.3. This range was limited by the width of the CMOS sensor. In other words, beyond 33.5°, the beam was no longer incident on the detector. Even still, though it is impossible to collect data near the asympote, the asymptotic behaviour is clear. Furthermore, the data agrees extremely well with the theory. The theory curve overlaps the experimental data almost perfectly.

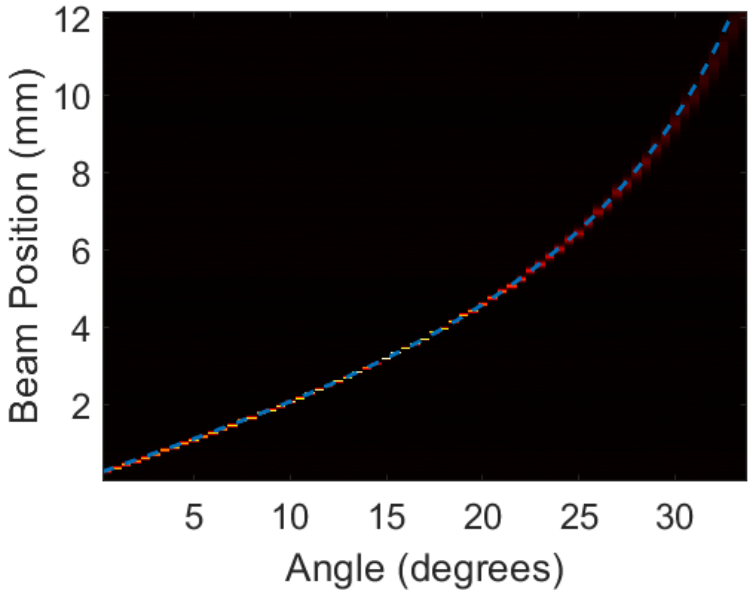

Figure 4.3: Experimental data of the beam walk-off through an airplate. The blue dashed line is the theory.

4.5 Image Shift

Since image planes are similar to focal planes, we can apply the same equations as we did for the beam waist shift measurements. This data will also give us a reference for the image quality and how it is affected by the glycerol and by the airplate. First, let's look at the image formed through free space (Fig. 4.4.a). We can clearly observe the individual printing dots. The image is not as colour saturated as the object likely due to the light source and the imperfect transmission through the optics.

Introducing the glycerol background medium results in a shift of the image along z by $\Delta_{\mathrm{HI}}^{\mathrm{CMOS}} = (+13.51 \pm 0.16)$ cm at the translation stage. According to theory, this should be $\Delta_{\mathrm{HI}}^{\mathrm{CMOS}} = +12.58$ cm. This theoretical value is not within the range of uncertainty and the experimental value has an percent error of 7.39 %. This is an acceptable error, especially given that we are expecting to get less reliable experimental shift values from the imaging measurements compared to the beam shift measurements, due to the the subjectivity in determining the position of the image plane. Again, the main purpose of the imaging measurements is to verify that this spaceplate is broadband in the visible and does not significantly affect the image quality at

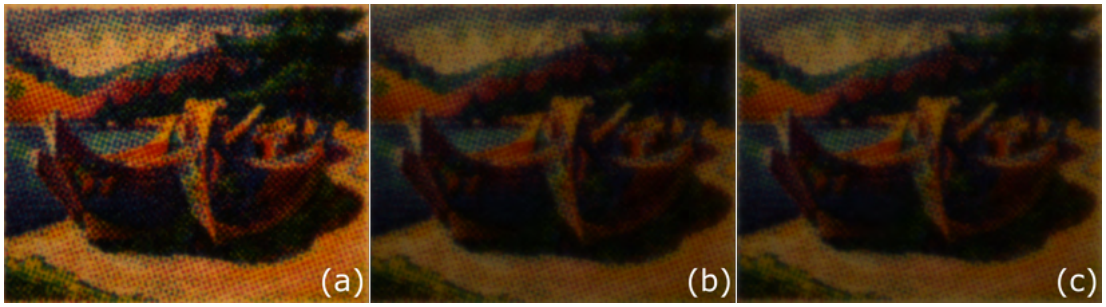

Figure 4.4: The image formed through **(a)** free space, **(b)** glycerol, and **(c)** the airplate.

low incident angles. Converting these values to those experienced at the tank, we have an experimental value of $\Delta_{\mathrm{HI}} = (+3.378 \pm 0.074)$ cm and a predicted value of $\Delta_{\mathrm{HI}} = 3.146$ cm.

Looking at Fig. 4.4.b, we see that the intensity of the image has decreased. This is due to the imperfect transmission spectrum of the glycerol. Additionally, the light propagates through 10 cm of this background medium, so there is likely a scattering effect as well. The printing dots are still individually visible.

Adding the airplate shifts the image plane $\Delta_{\mathrm{LI}}^{\mathrm{CMOS}} = (-1.58 \pm 0.18)$ cm, compared to the expected value of $\Delta_{\mathrm{LI}}^{\mathrm{CMOS}} = -1.402$ cm at the translation stage. The theoretical value lies within the uncertainty range of the experimental result, although it is at the very edge of that range. This image shift value agrees with theory because of the large depth of field. The percent error of 12.7 % is moderately large. Like with the beam shift data, we can convert these image shift values to those experienced prior to the 4f system, which is the more accurate representation of how much space has been compressed. With the introduction of the airplate, the image plane shifts by $\Delta_{\mathrm{LI}} = (-0.574 \pm 0.065)$ cm, compared to the predicted $\Delta_{\mathrm{LI}} = -0.5095$ cm.

Observing Fig. 4.4.c, we see that the image is not significantly different from the one in Fig. 4.4.b. This is expected, since all we have done is insert free space into the glycerol. Additionally, since this is a low NA system and the maximum incident angle is small, we expect no significant aberrations. This demonstrates that the airplate does not decrease image quality at low incident angles, however, other low-index spaceplates will likely affect the image differently.

In addition to taking measurements with an untilted airplate, we also wanted to observe the effect of imaging through a highly tilted airplate. Tilting the airplate allows us to simulate a system with high NA, like most common imaging systems. The photo in Fig. 4.5 was taken with

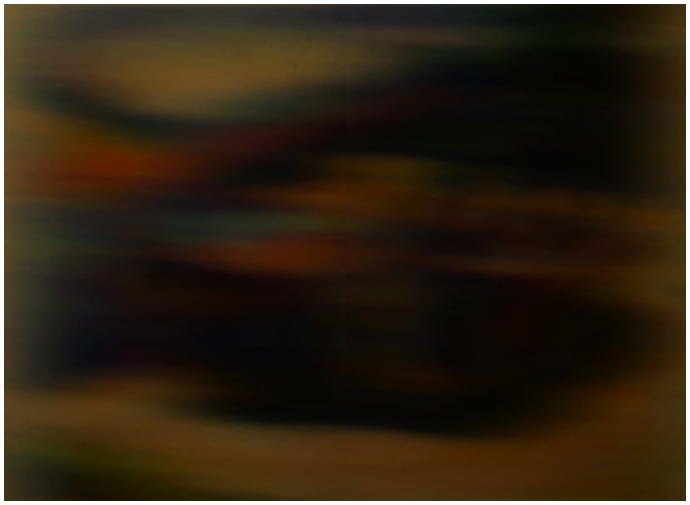

Figure 4.5: This is the most distinguishable image that formed through the highly tilted airplate. The image plane is neither flat nor cohesive.

an airplate tilt of 25°, near the position along z where the image plane should have formed. You may notice that the image is extremely out of focus. That is because the image plane cannot form through a low-index spaceplate at such high incident angles. Looking at Fig. 2.5, the plot of Eq. (2.28), we see that at 25°, the curve is not as flat as it is at smaller angles. This means that even with the small range of angles incident on the airplate, each ray of a different angle can experience very different shifts. As a result, no cohesive image plane forms.

Chapter 5

Experimental Demonstration of a Uniaxial Spaceplate

5.1 Design and Fabrication of Calcite Spaceplate

For the fabrication of our uniaxial spaceplate, we needed to consider the conditions found during our derivations. We also wanted to achieve as large a compression factor as possible, given by $\mathcal{R}_e = n_o/n_e$ in the simplified case where $n_{BG} = n_e$ and the incident angle is small. As such, we needed to consider negative uniaxial crystals with a large ratio between its two indices.

One such material is sodium nitrate ($NaNO_3$), which has a particularly high birefringence, resulting in a compression factor of $\mathcal{R}_e \approx 1.18$. However, it has not been able to be grown into large crystals until recently [30]. Furthermore, it is fairly brittle (2 on Mohs scale) and it is unclear if it can be cut and polished with the correct optic axis orientation.

As such, we have opted to use a calcite rectangular prism, since it has the greatest birefringence of any negative uniaxial material that is commercially available. Calcite's refractive indices are $n_e = 1.488 \pm 0.001$ and $n_o = 1.663 \pm 0.001$ at the wavelength of our laser, 532 nm. I rounded the indices to the decimal place where all of the data sets presented in Ref. [31] agreed. This would give us a compression factor of $\mathcal{R}_e = n_o/n_e = 1.118$, however, since the index of our background medium does not exactly match the extraordinary index of calcite (recall that $n_{BG} = 1.4537$), we can refine this compression factor to $\mathcal{R}_e = n_{BG}n_o/n_e^2 = 1.092$, giving a more modest compression of light propagation. Meanwhile, the ordinary polarization of light experiences $\mathcal{R}_o = n_{BG}/n_o = 0.8741$, which results in a beam waist shift in the positive z direction.

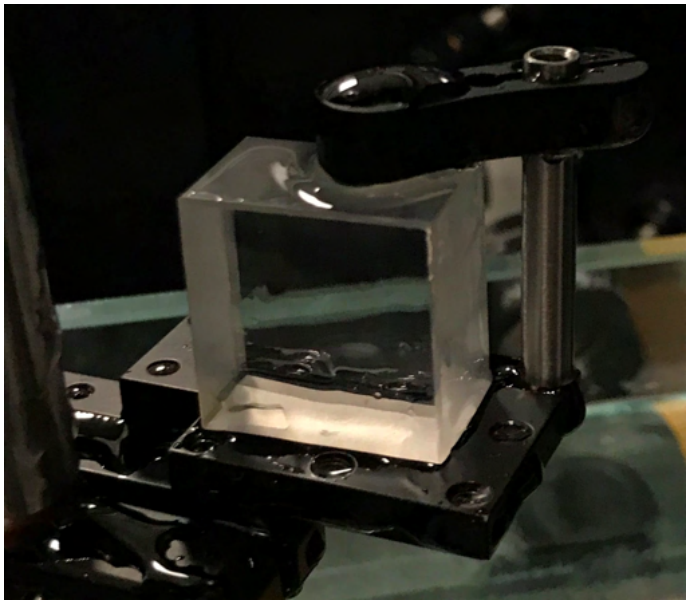

Figure 5.1: Photo of the calcite crystal, our uniaxial spaceplate used in experiments, immediately after being removed from the glycerol.

Looking at the wavelength-dependence of these indices, we can get an idea of whether this spaceplate is broadband in theory. Between the wavelengths of 380 nm and 750 nm (which bound the visible spectrum), the ordinary index of calcite changes by approximately 0.038, while the extraordinary index changes by only 0.017, based on data in Ref. [31]. This indicates that neither polarization of light will experience much chromatic aberration and that our desired e-polarization will experience slightly less chromatic aberration than the o-polarization. We will demonstrate the acceptable broadband performance of the calcite spaceplate in the context of visible-wavelength imaging. Though, chromatic aberrations may become more apparent when using a thicker spaceplate.

The calcite rectangular prism (Fig. 5.1) used in these measurements has a thickness of $d = (15.08 \pm 0.04)$ mm. This value was determined by taking the mean of 14 caliper measurements of the calcite spaceplate's thickness. The uncertainty is the standard error of that data set. This thickness was chosen such that in shift measurements it would be thick enough to provide a sufficiently large shift, while in the beam walk-off measurements it would be thin enough to transmit a larger range of angles. We did not use the thicker calcite crystal that we had used in Ref. [19], because the older thick calcite developed a film from being submerged in the flaxseed

oil for previous iterations of these measurements.

The manufacturer of our calcite crystals stated that the polish is of a poor quality due to the orientation of the optic axis. For both calcite prisms, there was a surface quality of 80-50 and a flatness of 5λ at 633 nm. The surface quality value uses the U.S. Military standard MIL-O-13830B, which is somewhat qualitative. In this system, 80-50 means that maximum scratch width is 80 microns and the digs (pits or chips in the crystal surface) have a maximum diameter of 0.50 mm.

Interestingly, Ref. [32] also notes that a calcite crystal with its optic axis oriented normal to the interface will focus radial polarized light and azimuthal polarized light at different positions, however, it does not recognize the spaceplate effect that arises when the crystal is submerged in an index-matching medium. Rather, they propose this as an easy method of generating these two polarizations.

5.2 Beam Waist Shift

We start with free space propagation, which will use the same data as presented in the previous chapter (Fig. 5.2.a). Again, it is included for completeness, rather than to prove the spaceplate concept. Since we are using the same background medium, we can also use the beam waist shift data from the glycerol measurement (Fig. 5.2.b). As a reminder, the shift of the beam waist from strictly free space propagation to propagation in glycerol was $\Delta_{\mathrm{HI}}^{\mathrm{CMOS}} = (+20.0 \pm 0.1)$ cm at the translation stage, compared to the predicted value of $\Delta_{\mathrm{HI}}^{\mathrm{CMOS}} = +19.66$ cm. At the tank, this converts to an experimental value of $\Delta_{\mathrm{HI}} = (+3.20 \pm 0.02)$ cm and a predicted value of $\Delta_{\mathrm{HI}} = 3.146$ cm.

Introducing the calcite spaceplate at 0° tilt will split the beam into two beams of different polarizations. Recall that the spaceplate must be tilted to isolate the two polarizations. For these measurements, we tilt the calcite by 7°, which is large enough to isolate the polarizations and is sufficiently small such that it will not change the theoretical values for beam waist shift. The e-polarized beam experienced a shift of $\Delta_{\mathrm{e}}^{\mathrm{CMOS}} = (-0.5 \pm 0.1)$ cm, as depicted in Fig. 5.2.c. The theoretical shift is $\Delta_{\mathrm{e}}^{\mathrm{CMOS}} = -0.5952$ cm. Converting these to the values at the tank, we find that the measured value is $\Delta_{\mathrm{e}} = (-0.12 \pm 0.02)$ cm, while the predicted value is $\Delta_{\mathrm{e}} = -0.1384$

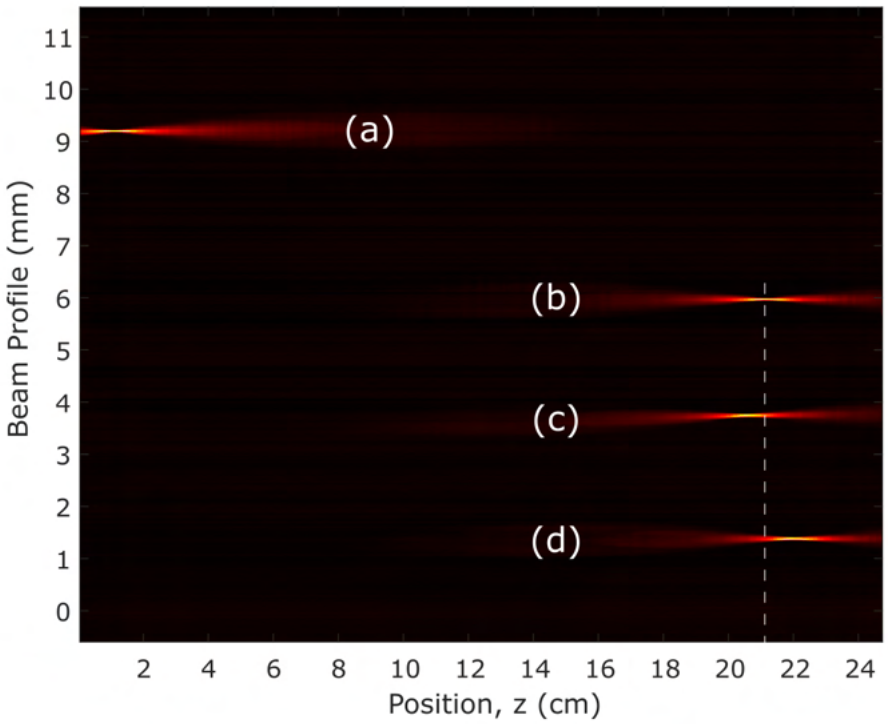

Figure 5.2: Experimental data depicting the profile of a beam through **(a)** only free space and **(b)** glycerol. **(c)** The e-polarized beam through calcite in glycerol. **(d)** The o-polarized beam through calcite in glycerol. The data from each trial has been superimposed into this figure and each beam's placement along the vertical axis is arbitrary. The white dashed line denotes the position of the beam waist through glycerol.

cm. This theoretical value lies withing the range of uncertainty, however the percent error of 16 % is particularly large.

The o-polarized beam, depicted in Fig. 5.2.d, experienced a shift of $\Delta_{\mathrm{o}}^{\mathrm{CMOS}} = (+0.9 \pm 0.1)$, whereas the theoretical shift is $\Delta_{\mathrm{o}}^{\mathrm{CMOS}} = +0.8160$ cm. At the tank, these values become $\Delta_{\mathrm{o}} = (+0.21 \pm 0.04)$ cm for the measured value and $\Delta_{\mathrm{o}} = +0.1898$ cm for the theoretical value. Again, this lies within the uncertainty, but the experimental value has a moderately large error of 10.3 %.

These relatively large errors could likely be rectified by taking measurements with a smaller step size. Other causes of this large error include the low compression factor and the small thickness of the calcite. We were able to achieve more accurate experimental results in Ref. [19] because we had used a calcite crystal with a larger thickness of $d \approx 30$ mm, which resulted in a more dramatic beam waist shift.

Additionally, the theoretical shift values for the high-index case were calculated with the approximation that the thickness of the background medium is 10.08 cm, which is the width of the tank including the glass. This is a reasonable approximation since the index of the glass is similar to the index of glycerol. However, since they are not exactly equal, this approximation may have contributed to the error.

Regardless, these measurements demonstrate the polarization dependence of the spaceplate effect in uniaxial spaceplates. In particular, it demonstrates that e-polarized light rays have been compressed by the uniaxial spaceplate, while the opposite effect occurs for o-polarized light. Importantly, these measurements agreed with theory within error.

5.3 Beam Walk-off

Using the same method as we did with the airplate, we take a photo for each 0.5° of spaceplate tilt about the y axis while the CMOS detector remains stationary at an arbitrary position near the beam waist. When a beam of light passes through our uniaxial spaceplate, it is split into two beams that will laterally shift in opposite directions as a function of spaceplate tilt. As we increase the tilt about y of the calcite crystal, we observe the beams translate in the x direction according to Eq. (2.24) for the e-ray and Eq. (2.25) for the o-ray. Unlike in the low-index case, we do not expect or observe any asymptotic behaviour. Although, for the e-polarized beam, we

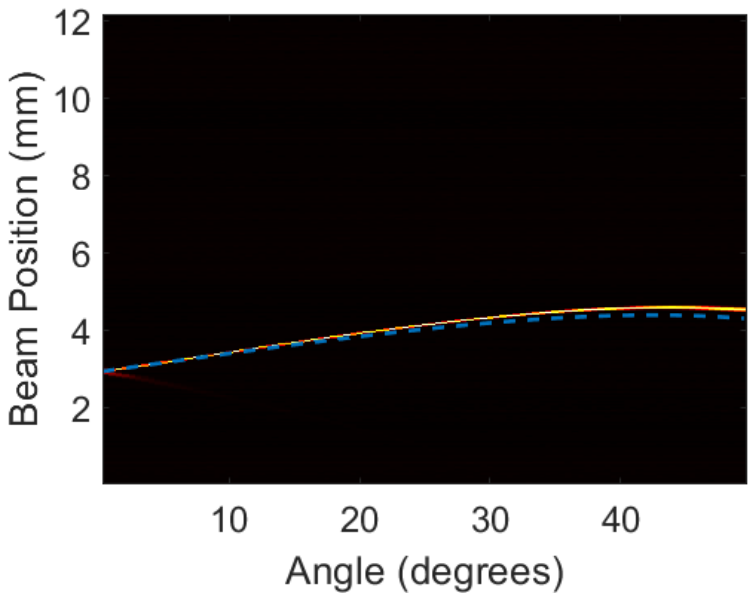

Figure 5.3: Experimental data of the e-polarized beam walk-off through the calcite spaceplate. The blue dashed line is the theory.

expect to see a change in direction for the walk-off at about 41°. In our data (Fig. 5.3), we observe the walk-off change direction at about 44°.

The e-ray walk-off is tested up to 49.5° while the o-ray was measured up to 62°. The maximum angle is limited by the geometry of the calcite crystal. The range of both polarizations can be expanded by decreasing d or by increasing the width of the calcite. The e-polarized beam transmits through at a smaller range of angles than the o-polarized beam because, in a uniaxial spaceplate, the e-rays bend away from the normal rather than towards it. This means that the e-rays will hit the side of the calcite at a smaller incident angle than the o-rays.

While our calcite walk-off data (Figs. 5.3 and 5.4) do not have as much agreement with theory as the airplate walk-off data, it is still in very good agreement. We can attribute the slight deviation at larger angles to the fact that the walk-off was not exactly in the x-z plane, but rather, travelled slightly in the y direction. This may have been due to the calcite being inadvertently tilted about the x or z axes. Furthermore, the calcite's optic axis may not be perfectly normal to the interface, thus affecting the walk-off.

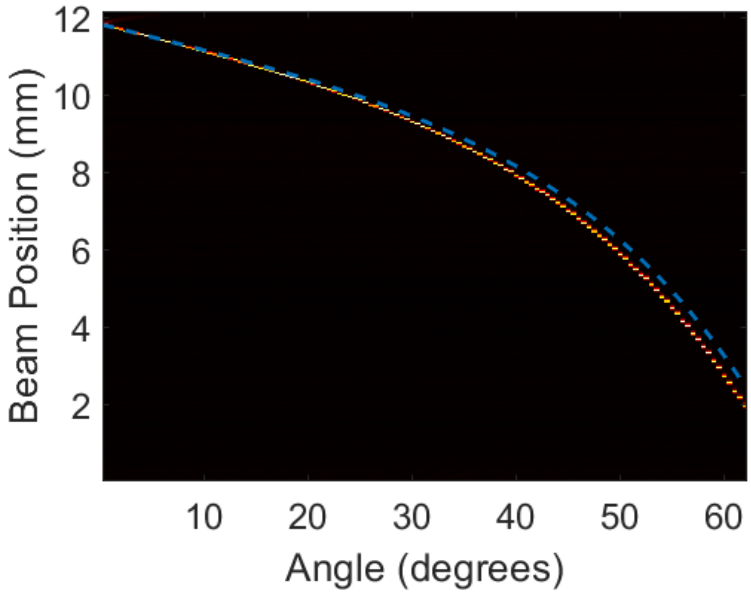

Figure 5.4: Experimental data of the o-polarized beam walk-off through the calcite spaceplate. The blue dashed line is the theory.

5.4 Image Shift

We use the same data from the free space propagation and from the glycerol propagation (Figs. 5.5.a and b). Recall that after the addition of glycerol, the image was shifted $\Delta_{\mathrm{HI}}^{\mathrm{CMOS}} = (+13.51 \pm 0.16)$ cm at the translation stage, compared to the theoretical $\Delta_{\mathrm{HI}}^{\mathrm{CMOS}} = +12.58$ cm. Converting to the values at the tank, the experimental value is $\Delta_{\mathrm{HI}} = (+3.20 \pm 0.02)$ cm and a predicted value is $\Delta_{\mathrm{HI}} = 3.146$ cm. Qualitative observations of these two images were made in the previous chapter.

Adding the calcite shifts the e-polarized image plane $\Delta_{\mathrm{e}}^{\mathrm{CMOS}} = (-0.38 \pm 0.18)$ cm, compared to the expected value of $\Delta_{\mathrm{e}}^{\mathrm{CMOS}} = -0.3809$ cm at the translation stage. At the tank, the experimental value is $\Delta_{\mathrm{e}} = (-0.14 \pm 0.07)$ cm and the expected value is $\Delta_{\mathrm{e}} = -0.1384$ cm. This result is particularly accurate, given that the measured image plane shifted by almost exactly the predicted distance and it's percent error of $0.236\,\%$ is the lowest of all our measured shift values.

Isolating the o-polarized image, we observe a shift of $\Delta_{\mathrm{o}}^{\mathrm{CMOS}} = (+0.61 \pm 0.23)$ cm, compared to a predicted value of $\Delta_{\mathrm{o}}^{\mathrm{CMOS}} = +0.5222$ cm. At the tank, the experimental value is $\Delta_{\mathrm{o}} =$

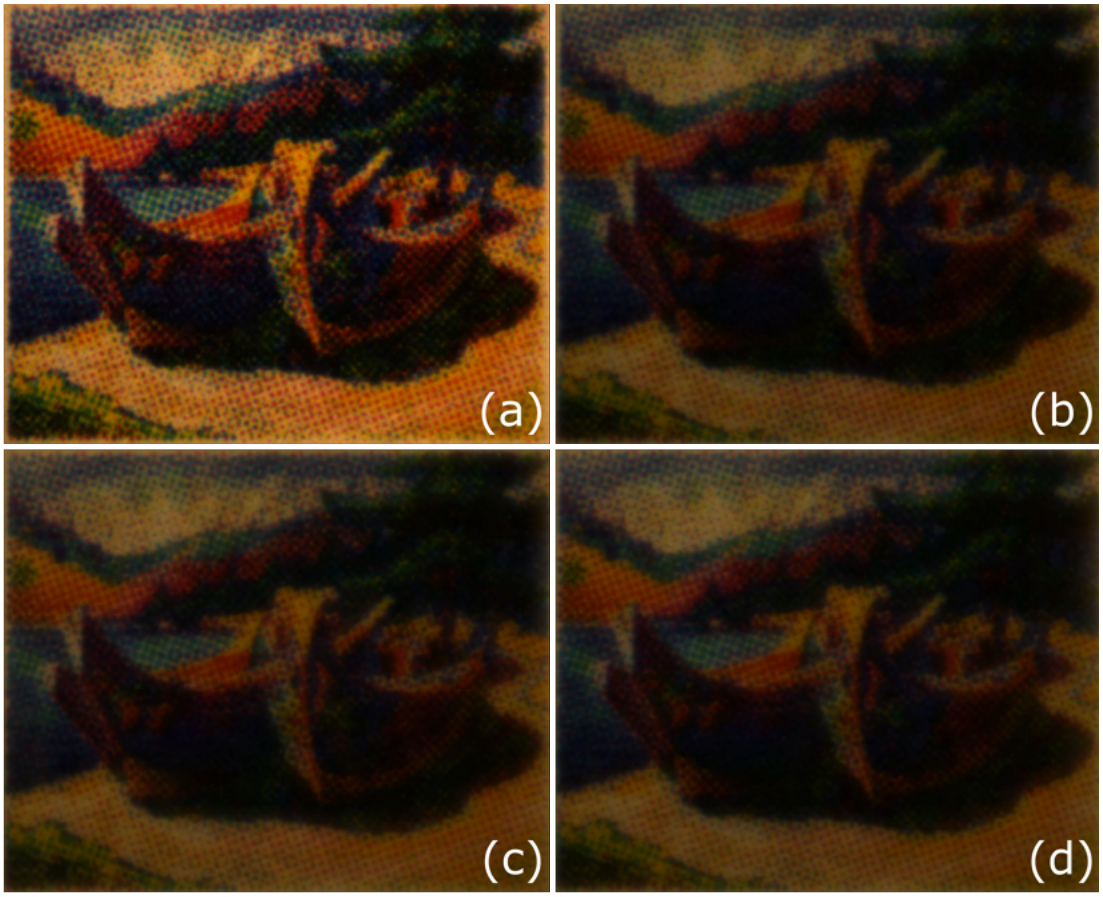

Figure 5.5: The image formed through **(a)** free space and **(b)** glycerol. **(c)** The e-polarized image formed through the calcite. **(c)** The o-polarized image formed through the calcite.

(+0.22±0.08) cm and the expected value is $\Delta_o = +0.1898$ cm. With a percent error of 16.8 %, this measurement was much less accurate than the e-polarized image shift measurement. However, the theoretical value of o-polarized image shift is well within the admittedly large uncertainty of the measurement. Again, all of the shift values for both the beam and image measurements are summarized in Table 6.1, converted to describe the shift in the tank, prior to the 4f system.

In terms of image quality, the e- and o-polarized images (Figs. 5.5.c and d) do not have any significant differences between them. This makes sense, given that we expect little to no monochromatic aberrations in our low NA system. Comparing these images to the one formed through glycerol (Fig. 5.5.b), we still do not observe any appreciable difference. This may be due to calcite's high transmission of visible wavelengths.

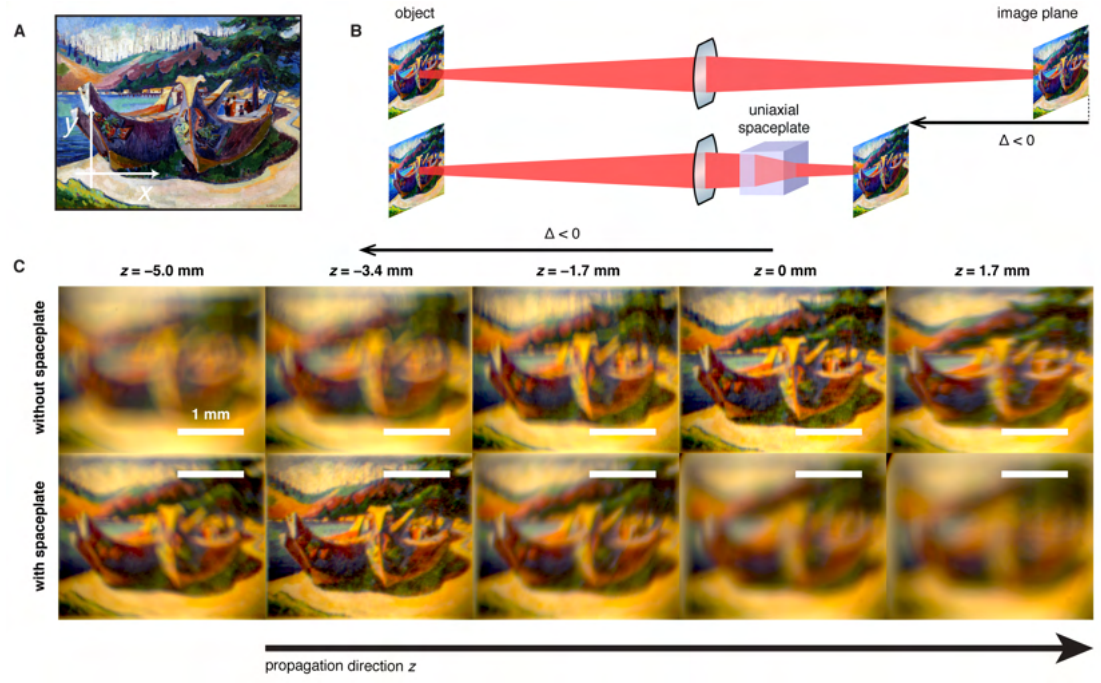

Figure 5.6: **(a)** The object being imaged. **(b)** A simplified version of the setup, demonstrating an image plane shift of $\Delta < 0$. **(c)** Photos taken at select positions along the path of the image. Here, the focus through glycerol (without spaceplate) has been defined as $z = 0$. Figure taken from Ref. [19].

To better demonstrate the quality of imaging that is possible through a calcite spaceplate, I've included Fig. 5.6 from our Nature Communications paper [19]. Using a calcite spaceplate of thickness $d = 29.84$ mm, we demonstrate a shift of $\Delta_e = -3.4$ mm in the tank, compared to a predicted $\Delta_e = -3.5$ mm. The printing dots are not as visible and the images are brighter. Both of these points are because a larger object was used and the imaging system had a lower overall magnification.

Imaging through highly tilted (25°) calcite, we see that the images of both polarizations fare much better than through the airplate. Both image planes form and the images are of decent quality. However, we observe that the e-polarized image (Fig. 5.7.a) is not as sharp as the o-polarized image (Fig. 5.7.b). In fact, we would have expected the o-polarized image to be less clear, since Δ_o changes more significantly as a function of θ_{BG} near 25° than Δ_e .

Additionally, we expect the o-polarization to have more monochromatic aberrations at high incident angles because its shift function $\Delta_o(\theta_{BG})$ is of the same form as that of a low-index

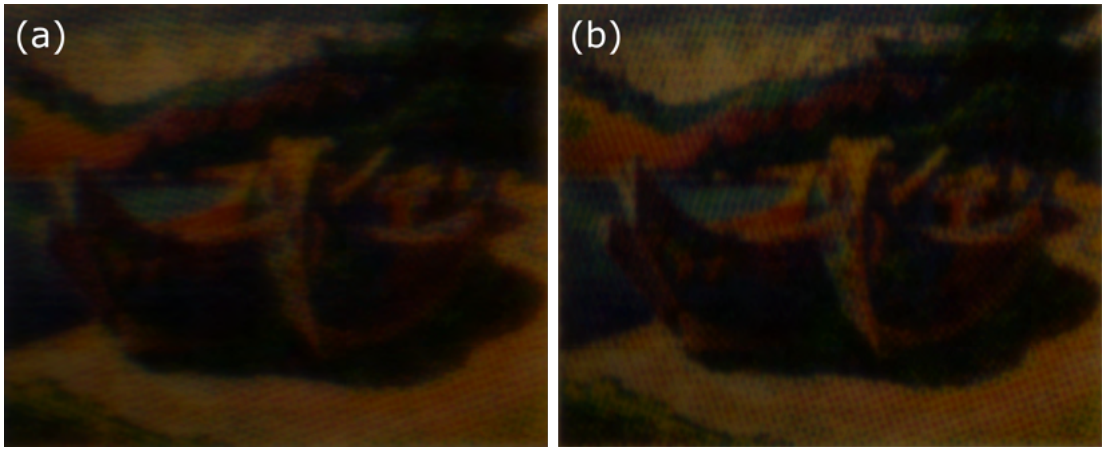

Figure 5.7: The images that formed after propagating through a highly tilted calcite spaceplate. **(a)** The e-polarized image. **(b)** The o-polarized image.

spaceplate. Although, we expect aberrations to be less severe for the o-polarized image than for the airplate image because the index contrast is lower. One possibility is that the e-rays may have interacted with the edge of the calcite at the exit face. Further investigation is needed to determine whether this is a deviation from our predictions or if it is due to an error. Regardless, the main purpose of this measurement was to demonstrate that uniaxial spaceplates are capable of imaging at high NA, while low-index spaceplates are not.

Chapter 6

Conclusion

In this thesis, we have experimentally demonstrated two proof of concept designs for spaceplates which replicate longer propagation distances of light within a background medium. The beam waist shift data, as well as the image shift data, has been summarized in Table 6.1 after being converted to describe the shift prior to the being longitudinally magnified by index change and by the 4f system. We see that some of our shift data agrees with theory within error. There were many values with unfortunately high percent errors. Generally, the larger shift values were more accurate. If these types of measurements were taken again, we would use spaceplates that demonstrate larger shifts. Additionally, we would use much smaller increments for the translation stage to obtain data with a smaller uncertainty.

Shift Type	Expt. Beam Shift (cm)	Theory (cm)	Expt. Image Shift (cm)
Δ_{HI}	$+3.20 \pm 0.02$	$+3.146$	$+3.378 \pm 0.074$
Δ_{LI}	-0.47 ± 0.02	-0.5095	-0.574 ± 0.065
Δ_{e}	-0.12 ± 0.02	-0.1384	-0.14 ± 0.07
Δ_{o}	$+0.21 \pm 0.04$	$+0.1898$	$+0.22 \pm 0.08$

Table 6.1: Beam and image shift results prior to the last 4f system. These values are the amount of space along the z axis that has been reduced (for negative values) or added (for positive values) via the introduction of a spaceplate. Note that the theoretical values apply to both the beam shift and the image shift measurements.

The walk-off that is characteristic of spaceplates was also verified experimentally. There was excellent agreement between data and theory for all three walk-off measurements. We also demonstrated that imaging through a spaceplate is possible and that the image quality is mostly unaffected when compared to propagation through glycerol, with the exception of low-index

spaceplates at high tilt. There was no noticeable chromatic aberration, though this should be verified quantitatively in the future.

6.1 Future Work

Much of the most promising future work that can be done on this topic is based on the development of other types of spaceplate. All of these spaceplates have the advantage of working in free space, which will be a critical feature of a viable spaceplate going forward.

6.1.1 Multilayer Spaceplates

Other individuals working on this project are developing multilayer spaceplates, however, this is beyond the scope of this thesis. As such, this will serve as a brief introduction to the topic. This type of spaceplate consists of a stack of alternating materials of varying thicknesses. It does not follow the general formula for homogeneous spaceplates, because it is a heterogeneous structure. Instead, it takes advantage of a complicated series of reflections between the layers, which result in the spaceplate effect.

In simulations, these types of spaceplates can achieve higher compression factors than the spaceplates presented in this thesis. In particular, the design from our Nature Communications paper achieves $\mathcal{R} = 4.9$, has a maximum acceptance angle of $\theta = 15°$ (NA=0.259), works in free space, and is polarization-independent [19]. One of the disadvantages is that it is not broadband; it only functions as intended for $\lambda = 1550$ nm, the wavelength for which it was designed. Additionally, this design has very low transmittance.

More recent multilayer spaceplate designs can achieve significantly larger compression factors, but often at the expense of polarization independence or large NA. For example, in Ref. [33], our group presents a design which has a remarkably high compression factor $\mathcal{R} = 340$, but with NA=0.017, which corresponds to a maximum angle of less than $\theta = 1°$. Designs like this would be useful in applications that have a low range of angles. Some of these designs have now been fabricated and will soon be tested.

6.1.2 ENZ Materials as Low-Index Spaceplates

The most promising potential low-index spaceplate would be made of an epsilon near zero (ENZ) material. Recall that $\mathcal{R}_{\text{LI}} = n_{\text{BG}}/n_{\text{SP}}$, so an arbitrarily high compression factor could be achieved using a material whose index of refraction can approach zero. Since the refractive index of these materials are below that of air, we could theoretically use these in free space, without the use of a high-index background medium. A spaceplate which can demonstrate a net improvement over free space propagation is the ultimate goal of this project.

Although, there are some considerations for the use of this type of spaceplate which limits their applications. Firstly, ENZ materials only have a sufficiently low index of refraction at a narrow range of wavelengths, though efforts have been made to make such devices more broadband [34,35]. As such, this would be best used in monochromatic applications, rather than broadband applications like colour imaging. Second, current ENZ materials are too lossy to be used in this context [36, 37]. Lastly, the range of incident angles that ENZ materials will accept decreases as ε approaches zero. Therefore, there is a clear trade-off between $\mathcal{R}$ and the maximum angle of incoming light.

6.1.3 Metamaterial Spaceplates

Recently, there have been publications which have demonstrated metamaterials which impart phase in a way that is angle-dependent [38,39]. It is possible for such metamaterials to perform the same operation as a spaceplate. This will be discussed in more detail in the following section. Alternatively, birefringent metamaterials could be used as uniaxial spaceplates and achieve much higher compression factors than what is possible using naturally occuring birefringent crystals.

6.2 Other Groups' Work

Recently, after the publication of our pre-print on this subject [40], at least two other groups have presented their own devices which have the same effect as a spaceplate. These designs were tested numerically using simulations. In both of these papers, neither group has physically built and tested their designs.

The first is Ref. [41], which proposes two designs of photonic crystals that would perform the same function as a spaceplate. A photonic crystal is a periodic dielectric nanostructure which forms energy bands for photons, similar to energy bands for electrons used in solid state physics. Their NA$\approx$ 0.01 design can have a compression factor of as much as $\mathcal{R} = 144$, while their NA$\approx$ 0.11 design has up to $\mathcal{R} = 38$. However, both of these designs are polarization-dependent; each polarization can experience vastly different compression factors.

The second, more recent publication is Ref. [42]. It describes an angle-dependent metasurface in order to achieve the spaceplate effect, as previously mentioned. Their designs can achieve compression factors of up to $\mathcal{R} = 5.6$ with NA=0.33. This paper describes a trade-off between maximum angular range θ_{max} and d_{eff} which applies to the devices from both papers,

$$\frac{d_{\text{eff}}}{\lambda} \sin^2 \theta_{\text{max}} = \frac{\mathcal{R}d}{\lambda} (\text{NA})^2 \leq 1 \,. \tag{6.1}$$

This explains why the lower NA design from the previous paper was able to achieve such a large compression factor.

In both of these cases, the term "spaceplate" was not used. It remains to be seen whether this term will become more widely used to describe this type of device. Although, the existence of these papers indicates that there may be an increasing interest in this topic of research. Hopefully, the use of spaceplates in commercial optical systems may be closer than we had previously thought.

Bibliography

[1] Rudolf Kingslake and R. Barry Johnson. *Lens design fundamentals*. Academic Press, second edition, 2010.

[2] Douglas C. Giancoli. *Physics: Principles with Applications*. Pearson Prentice Hall, sixth edition, 2005.

[3] Eugene Hecht. *Optics*. Pearson, fifth edition, 2017.

[4] W.T. Xie, Y.J. Dai, R.Z. Wang, and K. Sumathy. Concentrated solar energy applications using fresnel lenses: A review. *Renewable and Sustainable Energy Reviews*, 15(6):2588–2606, aug 2011.

[5] Cristina Sierra and Alfonso J. Vázquez. High solar energy concentration with a fresnel lens. *Journal of Materials Science*, 40(6):1339–1343, mar 2005.

[6] Kiseung Bang, Youngjin Jo, Minseok Chae, and Byoungho Lee. Lenslet VR: Thin, flat and wide-FOV virtual reality display using fresnel lens and lenslet array. *IEEE Transactions on Visualization and Computer Graphics*, 27(5):2545–2554, may 2021.

[7] A. Nikonorov, M. Petrov, S. Bibikov, Y. Yuzifovich, P. Yakimov, N. Kazanskiy, R. Skidanov, and V. Fursov. Comparative evaluation of deblurring techniques for fresnel lens computational imaging. In *2016 23rd International Conference on Pattern Recognition (ICPR)*. IEEE, dec 2016.

[8] Nanfang Yu, Patrice Genevet, Mikhail A Kats, Francesco Aieta, Jean-Philippe Tetienne, Federico Capasso, and Zeno Gaburro. Light Propagation with Phase Discontinuities: Generalized Laws of Reflection and Refraction. *Science*, 334(6054):333–337, 2011.

[9] Francesco Aieta, Patrice Genevet, Mikhail A. Kats, Nanfang Yu, Romain Blanchard, Zeno Gaburro, and Federico Capasso. Aberration-free ultrathin flat lenses and axicons at telecom wavelengths based on plasmonic metasurfaces. *Nano Letters*, 12(9):4932–4936, aug 2012.

[10] Adeel Afridi, Josep Canet-Ferrer, Laurent Philippet, Johann Osmond, Pascal Berto, and Romain Quidant. Electrically Driven Varifocal Silicon Metalens. *ACS Photonics*, 2018.

[11] Shuming Wang, Pin Chieh Wu, Vin-Cent Su, Yi-Chieh Lai, Mu-Ku Chen, Hsin Yu Kuo, Bo Han Chen, Yu Han Chen, Tzu-Ting Huang, Jung-Hsi Wang, Ray-Ming Lin, Chieh-Hsiung Kuan, Tao Li, Zhenlin Wang, Shining Zhu, and Din Ping Tsai. A broadband achromatic metalens in the visible. *Nature Nanotechnology*, 13(3):227–232, jan 2018.

[12] M. Khorasaninejad, W. T. Chen, R. C. Devlin, J. Oh, A. Y. Zhu, and F. Capasso. Metalenses at visible wavelengths: Diffraction-limited focusing and subwavelength resolution imaging. *Science*, 352(6290):1190–1194, 2016.

[13] Gwanho Yoon, Kwan Kim, Daihong Huh, Heon Lee, and Junsuk Rho. Single-step manufacturing of hierarchical dielectric metalens in the visible. *Nature Communications*, 11(1), may 2020.

[14] Xin Yu, Yun Shen, Guohong Dai, Liner Zou, Tailin Zhang, and Xiaohua Deng. Phase-controlled planar metalenses for high-resolution terahertz focusing. *Photonics*, 8(5):143, apr 2021.

[15] Wei Ting Chen, Alexander Y. Zhu, Vyshakh Sanjeev, Mohammadreza Khorasaninejad, Zhujun Shi, Eric Lee, and Federico Capasso. A broadband achromatic metalens for focusing and imaging in the visible. *Nature Nanotechnology*, 13(3):220–226, mar 2018.

[16] M. Khorasaninejad, W. T. Chen, A. Y. Zhu, J. Oh, R. C. Devlin, D. Rousso, and F. Capasso. Multispectral chiral imaging with a metalens. *Nano Letters*, 16(7):4595–4600, jun 2016.

[17] Ren Jie Lin, Vin-Cent Su, Shuming Wang, Mu Ku Chen, Tsung Lin Chung, Yu Han Chen, Hsin Yu Kuo, Jia-Wern Chen, Ji Chen, Yi-Teng Huang, Jung-Hsi Wang, Cheng Hung Chu, Pin Chieh Wu, Tao Li, Zhenlin Wang, Shining Zhu, and Din Ping Tsai. Achromatic metalens array for full-colour light-field imaging. *Nature Nanotechnology*, 14(3):227–231, jan 2019.

[18] Niklas Kröger, Jochen Schlobohm, Andreas Pösch, and Eduard Reithmeier. Using refraction in thick glass plates for optical path length modulation in low coherence interferometry. *Applied Optics*, 56(25):7299, sep 2017.

[19] Orad Reshef, Michael P. DelMastro, Katherine K. M. Bearne, Ali H. Alhulaymi, Lambert Giner, Robert W. Boyd, and Jeff S. Lundeen. An optic to replace space and its application towards ultra-thin imaging systems. *Nature Communications*, 12(1), June 2021.

[20] Joseph W. Goodman. *Fourier Optics*. Roberts & Company, Englewood, Colorado, third edition, 2005.

[21] Sourangsu Banerji, Monjurul Meem, Apratim Majumder, Fernando Guevara Vasquez, Berardi Sensale-Rodriguez, and Rajesh Menon. Imaging with flat optics: metalenses or diffractive lenses? *Optica*, 6(6):805–810, 2019.

[22] Augustin-Jean Fresnel. *Oeuvres complètes d'Augustin Fresnel*. Nineteenth Century Collections Online (NCCO): Science, Technology, and Medicine: 1780-1925. Imprimerie Impériale, Paris.

[23] Kenro Miyamoto. The phase Fresnel lens. *Journal of the Optical Society of America*, 51(1):17–20, 1961.

[24] Robert W. Boyd. *Nonlinear Optics*. Academic Press, fourth edition, 2020.

[25] S Roshan Entezar and M Karimi Habil. Refraction and reflection from the interface of anisotropic materials. *Physica Scripta*, 94(8):085502, aug 2019.

[26] Xinyue Han, Dengshuai Xue, Jun Zheng, Sami M. Alelyani, and Xiaobin Chen. Spectral characterization of spectrally selective liquid absorption filters and exploring their effects on concentrator solar cells. *Renewable Energy*, 131:938–945, feb 2019.

[27] LF Hoyt. New table of the refractive index of pure glycerol at 20 c. *Industrial & Engineering Chemistry*, 26(3):329–332, 1934.

[28] *ICUMSA Method SPS-3 (2000) Refractometry and Tables*. International Commission for Uniform Methods of Sugar Analysis, 2000.

[29] R. D. Birkhoff, L. R. Painter, and J. M. Heller. Optical and dielectric functions of liquid glycerol from gas photoionization measurements. *The Journal of Chemical Physics*, 69(9):4185–4188, nov 1978.

[30] Wei Xiong, Liang Chen, Lingxiong Huang, Feiyun Guo, Yao Zhou, and Hui Yuan. Bridgman growth and characterization of birefringent crystal NaNO3. *Crystal Research and Technology*, 50(3):250–254, mar 2015.

[31] Gorachand Ghosh. Dispersion-equation coefficients for the refractive index and birefringence of calcite and quartz crystals. *Optics Communications*, 163(1-3):95–102, may 1999.

[32] Miklós Erdélyi and Gábor Gajdátsy. Radial and azimuthal polarizer by means of a birefringent plate. *Journal of Optics A: Pure and Applied Optics*, 10(5):055007, 2008.

[33] Jordan T. R. Page, Orad Reshef, Robert W. Boyd, and Jeff S. Lundeen. Designing high-performance propagation-compressing spaceplates using thin-film multilayer stacks. 2021.

[34] L. Sun and K. W. Yu. Strategy for designing broadband epsilon-near-zero metamaterials. *Journal of the Optical Society of America B*, 29(5):984, apr 2012.

[35] Ruben Maas, James Parsons, Nader Engheta, and Albert Polman. Experimental realization of an epsilon-near-zero metamaterial at visible wavelengths. *Nature Photonics*, 7(11):907–912, 2013.

[36] Nader Engheta. Pursuing near-zero response. *Science*, 340(6130):286–287, apr 2013.

[37] Daryl I. Vulis, Orad Reshef, Philip Camayd-Muñoz, and Eric Mazur. Manipulating the flow of light using Dirac-cone zero-index metamaterials. *Reports on Progress in Physics*, 82(1):012001, jan 2019.

[38] Xiyue Zhang, Qi Li, Feifei Liu, Meng Qiu, Shulin Sun, Qiong He, and Lei Zhou. Controlling angular dispersions in optical metasurfaces. *Light: Science & Applications*, 9(1), may 2020.

[39] Zhujun Shi, Alexander Y. Zhu, Zhaoyi Li, Yao-Wei Huang, Wei Ting Chen, Cheng-Wei Qiu, and Federico Capasso. Continuous angle-tunable birefringence with freeform metasurfaces for arbitrary polarization conversion. *Science Advances*, 6(23):eaba3367, jun 2020.

[40] Orad Reshef, Michael P. DelMastro, Katherine K. M. Bearne, Ali H. Alhulaymi, Lambert Giner, Robert W. Boyd, and Jeff S. Lundeen. Towards ultra-thin imaging systems: an optic to replace space. 2020.

[41] Cheng Guo, Haiwen Wang, and Shanhui Fan. Squeeze free space with nonlocal flat optics. *Optica*, 7(9):1133, 2020.

[42] Aobo Chen and Francesco Monticone. Dielectric nonlocal metasurfaces for fully solid-state ultrathin optical systems. *ACS Photonics*, 8(5):1439–1447, may 2021.